A comprehensive study of Surface Water and Ocean Topography (SWOT) Pixel Cloud data for flood extent extraction

Quentin Bonassies, Christophe Fatras, Santiago Peña-Luque, Pierre Dubois, Andrea Piacentini, Ludovic Cassan, Sophie Ricci, Thanh Huy Nguyen

Remote Sensing of Environment 333 (2026) 115101

Contents lists available at ScienceDirect

Remote Sensing of Environment

journal homepage: www.elsevier.com/locate/rse

A comprehensive study of Surface Water and Ocean Topography (SWOT) Pixel Cloud data for flood extent extraction

Quentin Bonassies [a,d,*], Christophe Fatras [b], Santiago Peña-Luque [c], Pierre Dubois [b], Andrea Piacentini [d], Ludovic Cassan [a,d], Sophie Ricci [a,d], Thanh Huy Nguyen [e]

[a] Univ Toulouse, CNRS/Cerfacs/IRD, CECI, 42 av. Gaspard Coriolis, Toulouse, 31100, France
[b] Collecte Localisation Satellites, 11 Rue Hermès, Ramonville-Saint-Agne, 31520, France
[c] CNES, 8 av. Edouard Belin, Toulouse, 31400, France
[d] CERFACS, 42 av. Gaspard Coriolis, Toulouse, 31100, France
[e] Luxembourg Institute of Science and Technology, 5 av. des Hauts-Fourneaux, Esch-sur-Alzette, L-4362, Luxembourg

ARTICLE INFO

Edited by Menghua Wang

Keywords:
Remote sensing
Surface Water and Ocean Topography (SWOT)
Flood extent
Interferometric coherence
Radar
Ka-band Radar Interferometer (KaRIn)

ABSTRACT

Current disaster and emergency management services produce flood maps within hours using satellite data. To handle large-scale events efficiently, a reliable automated method is needed to generate an initial flood extent map, which can then be refined manually.

Launched in December 2022, the Surface Water and Ocean Topography (SWOT) satellite, equipped with the Ka-band Radar Interferometer (KaRIn), provides high-resolution radar observations used here for flood detection. While not initially designed for detailed flood mapping in vegetated or urban regions, the performance of SWOT's Pixel Cloud products was assessed during four major flood events in Greece, France, Brazil, and the USA. Each event is paired with Sentinel-1 or Sentinel-2 imagery within a 3-hour time frame, providing a valuable opportunity to compare and evaluate SWOT's flood detection capabilities.

Three radar variables of the Pixel Cloud products are studied for extracting flood extents: σ_0, coherent power, and interferometric coherence — which is computed from the two complex interferograms. They are compared to the built-in classification and flood masks computed from Sentinel-1/2. The study demonstrates the capabilities of the SWOT satellite in detecting flooded vegetation, flooded urban areas, and even regions with high snow cover. However, limitations are observed: (1) when high soil moisture is observed, causing signal saturation, (2) SWOT can be sensitive to the incidence angle, both of which lead to less reliable flood extent estimation. These findings highlight the potential of SWOT satellite for improving global flood mapping, as well as the need for further exploration to address current limitations and enhance flood monitoring capabilities in the near future.

1. Introduction

Floods are the most frequent natural disasters in the world. Their frequency and severity have more than doubled in the past 20 years, with strong social and economic impact (UNDRR, 2021). To effectively anticipate, monitor, and mitigate the impacts of such disasters, reliable, timely, and large-scale observation tools are essential. Modeling and prediction of these events are key tools for their efficient monitoring. Earth observation (EO) satellite data, hydrological and hydraulic models, along with data assimilation (DA) systems, have become essential tools for monitoring flood events (Bates, 2022; Jafarzadegan et al., 2023). Several operational systems have been developed to support flood monitoring and emergency response, including NASA Disaster Response Coordination System (DRCS) and the Copernicus Emergency Management Service (CEMS), which provides rapid flood mapping and risk assessments from satellite imagery. The Global Flood Awareness System (GloFAS), part of the CEMS, is an operational platform for global flood monitoring and forecasting. It delivers daily flood forecasts and monthly seasonal streamflow outlooks worldwide (Harrigan et al., 2020; Prudhomme et al., 2024).

In this context, the Surface Water and Ocean Topography (SWOT) mission – launched by NASA and CNES in December 2022 – represents a major advancement in satellite-based hydrology (Fu et al., 2024; Getirana et al., 2024). Complementary to traditional optical or radar sensors, SWOT employs Ka-band (35.75 GHz/8.3858 mm) Radar Interferometry (KaRIn) with two antennas with a 10 m baseline and a low-incidence (0.6 ° - 3.9 ° off-nadir) angle configuration, enabling

* Corresponding author.
E-mail address: quentin.bonassies@cerfacs.fr (Q. Bonassies).

https://doi.org/10.1016/j.rse.2025.115101
Received 16 July 2025; Received in revised form 20 October 2025; Accepted 21 October 2025
Available online 5 November 2025

direct and highly-resolved measurements of inland water surface features (heights, radiometry, extent, slope and storage variation) over two 50-kilometers-wide swaths at every pass of its scientific orbit ((J.P.L. D-109532), 2024). For flood monitoring, it is essential to observe the floodplains and extract the flood extent. SWOT global revisit cycle is of 21 days, during which sites are revisited 2–4 times at irregular intervals, with observation frequency increasing with latitude and decreasing near the equator (Biancamaria et al., 2016). This revisit period can make flood observation with SWOT challenging, yet it still adds a new type of observation to the satellite constellation for flood monitoring and mapping. Among SWOT's products, the Pixel Cloud (PIXC) product (SWOT, 2023) provides access to raw geolocalized interferometric signals at the sensor's native resolution (~10–70 m cross-track, ~5–10 m along-track), making it particularly promising for fine-scale flood extent mapping. Those flood extent maps can be combined with hydrological and hydraulic models to enhance the predictive and diagnostic capabilities of flood forecasting systems (Hostache et al., 2018; Dasgupta et al., 2021b).

Flood forecasting and inundation mapping rely heavily on numerical hydrodynamic models (e.g., LISFLOOD-FP, ISBA-CTRIP, HEC-RAS, TELEMAC) that simulate rainfall-runoff, river hydraulics, and floodplain dynamics (Hostache et al., 2018; Grimaldi et al., 2016; Emery et al., 2020; Nguyen et al., 2023). These models can be enhanced through DA techniques, which integrate EO data–such as altimetry, flood extents, and backscatter–to reduce uncertainty and improve real-time forecasting (Bates and De Roo, 2000; Moradkhani et al., 2005; Schumann et al., 2008; Oubanas et al., 2018; Dasgupta et al., 2021b; Di Mauro et al., 2021; Nguyen et al., 2022a; Bonassies et al., 2025). EO-derived flood masks are central to these systems, generated using various methods ranging from simple thresholding and water indices to advanced machine learning (ML) approaches like FloodML (Kettig et al., 2021). Sentinel-1 (C-band Synthetic Aperture Radar (SAR)) and Sentinel-2 (optical sensor) are widely used due to their complementary capabilities: Sentinel-1 provides all-weather, day-night SAR imagery, but struggles in urban and vegetated areas, while Sentinel-2 offers high-resolution optical data but is constrained by cloud cover, vegetation cover and acquisition timing (Dasgupta et al., 2021a; Nguyen et al., 2022b; García-Pintado et al., 2015). When available, optical imagery adds valuable contextual information for flood mapping and impact assessment. The SWOT mission, with its KaRIn sensor, offers a promising advancement by enabling surface water detection even under vegetation or within urban environments. However, the presence of signal noise in SWOT data, as well as false signals, such as the omission of true water surfaces due to the "dark water" phenomenon and false positives from urban "bright land" effects, highlights the need for careful interpretation during flood events, especially in cases of river overflow.

The terrestrial hydrological system is highly complex, and the SWOT High-Rate (HR) mode provides a variety of products to support its monitoring. Numerous studies were conducted to prepare this mission (Wongchuig-Correa et al., 2020; de Moraes Frasson, 2021; Durand et al., 2023). SWOT offers a multitude of products. The Pixel Cloud (level-2 product) provides a non-structural geolocalized point cloud of high-resolution KaRIn data. Water bodies such as rivers, lakes, wetlands, and floodplains are then identified and processed into more user-friendly products, including Level-2 River Node and Reach, Lake, and Raster products (at 100 and 250 m resolution). Node and Reach River products provide average estimates of water surface elevation (WSE), slopes, width, area, and discharges on a Node (approx. 200 m spacing) or a Reach (approx. 10 km spacing) along a centerline defined in the Prior River Database, the SWORD database (Altenau et al., 2021). Since SWOT launch in December 2022, some studies work on assessing the accuracy of SWOT products for hydrology (*e.g.* Maubant et al. (2025)). Other studies have used Nodes and Reach products for global hydrology integration in numerical models or DA systems. It is used for water slope calculation, WSE along the river centerlines, or water flow computation and event comprehension (Laipelt et al., 2025; Oubanas et al., 2024; Rezende et al., 2025; Yu et al., 2024; Andreadis et al., 2025). Others analyze Lakes products to monitor the hydrology cycles of lakes and reservoirs (Hamoudzadeh et al., 2024; Yu et al., 2024). Some papers use the PIXC product to study flood events by selecting water-classified pixels and performing an extrapolation with Digital Elevation Model (DEM) (Simoes-Sousa et al., 2025). PIXC or Nodes products are used for WSE validation, topography, or bathymetry retrievals (He et al., 2025; Salameh et al., 2024; Rezende et al., 2025). However, some of them use native PIXC classification as the water mask reference, without further questioning its validity, which, by extrapolation, could add errors due to the DEM hypothesis and resolution.

One key variable for defining Reach, Nodes, or Lakes products is the classification. It is computed from KaRIn radar variables and provides information on the observed surface type (water, water near land, land). However, this classification is not perfect, and some bias and errors are observed in the current SWOT-HR release (version C). Version D is under release, but the HR products have not been yet reprocessed (SWOT, 2025). The PIXC also contains the raw interferometric variables such as the backscattering coefficient (also called sigma nought or σ_0), the coherent power ($P_{coherent}$) and the complex interferogram ((J.P.L. D-109532), 2024; (J.P.L. D-105504), 2023). From the two complex interferograms of the two antennas, the interferometric coherence (γ_{total}) can be computed. Those variables are highly sensitive to water detection and are used to compute more comprehensive variables, such as the classification or WSE for example. In oceanography, interferometric coherence is a well-established parameter – particularly from SWOT Low-Rate data designed for ocean observation – that serves as a reliable proxy for estimating significant wave height and provides valuable insights into wave spectral energy (Bohé et al., 2025). In this article, the SWOT backscattering coefficient, coherent power, and interferometric coherence are analyzed and utilized to compute water masks using a simple histogram thresholding method.

SWOT's KaRIn sensor is a groundbreaking technology for the hydrology community, yet its full potential for flood monitoring remains to be thoroughly understood. While some initial studies (Laipelt et al., 2025; Simoes-Sousa et al., 2025; Andreadis et al., 2025; Salameh et al., 2024) have explored the River (PIXC, Node and Reach) products, a comprehensive understanding of KaRIn's behavior during flood events – particularly for accurate flood extent extraction – remains limited. Current applications of the PIXC product often depend on selecting only confidently classified pixels (Nguyen et al., 2024), raising important questions about its reliability under less-than-ideal conditions. For example, how well does PIXC perform in densely vegetated or urban areas? Can it detect floods during snow cover or in the presence of high soil moisture, especially during the flood recession phase? Is the built-in classification adequate for flood detection, or are additional variables needed? To investigate these questions, four major flood events were selected from SWOT's science orbit data, occurring between 2023 and 2025 in France, Brazil, Greece, and the United States. Each event is paired with a corresponding Sentinel-1 or Sentinel-2 image taken within a 3-hour timeframe, which serves as a reference for qualitative flood extent. This paper presents the datasets used, the methods developed for SWOT data processing and classification into our flood extent masks, and comparative analyses with established EO sources, as well as with the SWOT built-in classification. Through this, we aim to evaluate the capabilities and limitations of SWOT for flood mapping and provide insights for future research and operational use.

2. Data

2.1. Sentinel-1 and Sentinel-2 data

Four flood events have been selected for this study because each of them has a Sentinel-1 or Sentinel-2 image within a maximum 2.5-hour interval with a SWOT acquisition. Thanks to the many years

Table 1
Comparison between available satellite data for the four flood events.

Event	Comparison with	Date of image (UTC)	Time difference	SWOT image date (UTC)	Cloud coverage	Flood peak
Chinon, France	Sentinel-1	2024-03-31 17:48	- 02:32	2024-03-31 15:16	–	2024–04–01
Porto Alegre, Brazil	Sentinel-2	2024-05-06 13:31	- 01:45	2024-05-06 11:46	≈ 2 %	2024-05-05
Owensboro, USA	Sentinel-2	2025-02-20 16:32	+ 01:30	2025-02-20 18:02	≈ 50 % (on the global tile)	2025-02-21
Farkadona, Greece	Sentinel-2	2023-09-15 09:20	- 02:12	2023-09-15 07:08	≈ 15 %	2023-09-05

Table 2
Comparison of SWOT sensor characteristics with Sentinel-1 and Sentinel-2 satellites.

	SWOT	Sentinel-1	Sentinel-2
Sensors	KaRIn instrument	C-SAR instrument	Multi-Spectral Instrument
Revisit cycle	21 days	12 days	10 days
Constellation revisit cycle (nominal configuration)	21 days	6 days (region dependent)	5 days
Bandwidth	Ka-band (35.75 GHz/8.3858 mm)	C-band (4-8 GHz/3.8-7.5 cm)	Multi-spectral (13 spectral channels between visible, near infrared and short wave infrared)
Incidence angle	0.6 ° - 3.9 °	29.1 ° - 46.0 ° (Interferometric Wide Swath mode)	0 ° - 20 ° (Zenithal Viewing Angle)
Swath width	two 50-km-wide swaths	250 km	290 km
Resolution	10–70 × 5–10 m	20 × 22 m (Interferometric Wide Swath mode)	10, 20 or 60 m

of experience with the Sentinel-1 and Sentinel-2 data in the context of flood observation, we can rely on a consolidated interpretation of the selected images. Table 1 shows the available images in each case, with the time difference between SWOT and the comparison images. The time gap observed with SWOT is negligible in the case of those major flood events. Table 2 shows the main characteristics of the three satellite sensors. SWOT incidence angle and bandwidth are a novelty in radar for hydrology studies.

2.1.1. Sentinel 1

Sentinel-1 is the SAR component of the ESA's Copernicus program. It is composed of a constellation of satellites in orbit since 2014 that provide high-resolution, all-weather, day-and-night imaging, making them essential for monitoring Earth's surface. The data is widely used for applications such as disaster management, particularly for monitoring flood events (Twele et al., 2016; Martinis et al., 2018). For our study, Sentinel-1 A acquisitions cover the Chinon (France) flood event of March 31st, 2024 (Fig. 1 [a]) only 2 h and 32 min after the SWOT measurement made over this study site, making it an almost synchronous observation of the same flood extent.

2.1.2. Sentinel 2

Sentinel-2 is the high-resolution multi-spectral imaging component of the ESA's Copernicus program. The Sentinel-2 constellation, in orbit since 2016, captures high-resolution optical imagery in several spectral bands, making the data valuable for monitoring land cover, vegetation, water bodies, and urban areas. It is highly sensitive to cloud cover for flood monitoring. Nevertheless, it provided an almost cloudless coverage (see Table 1) of the Porto Alegre (Brazil) flood event close to its peak extent on May 6th, 2024, at 13h31 UTC (see Fig. 1 [b]), that is only 1h45 after SWOT measurement on the same area (11h46). It also provided more cloudy but usable images of Owensboro (USA - Fig. 1 [c]) and Farkadona (Greece - Fig. 1 [d]) study cases. In Owensboro study area, a major part of the area of interest is covered by snow. However, the flooded areas are still easily visible. The flood in Greece is located in the northern part of the image (Fig. 1 [d]). The flood is difficult to observe in both SWOT and Sentinel-2 images on this date, as it was acquired during the flood recession with high soil moisture within cropland areas. Although the SWOT and Sentinel-2 images were less optimal than in other cases, the Greece case captures the post-peak phase of a flood event—a critical period for studying potential residual flood traces and understanding the event's progression.

2.2. Study sites

The localization of the areas of interest (AOI) and SWOT passes for the four selected flood events is shown in Fig. 2. For the remainder of the study, the events will be referred to as follows: Chinon, France; Porto Alegre, Brazil; Owensboro, USA; and Farkadona, Greece.

The Chinon (France) flood event is a recurring phenomenon, as the area is often flooded at this time of year. This particular flood event is particularly intense, filling almost the entire floodplain. The Porto Alegre flood event (Brazil), which occurred in April and May 2024, resulted from a combination of atmospheric conditions that generated prolonged and intense rainfall (Simoes-Sousa et al., 2025). This extreme flood event is related to the EMSN 194[1] of the Copernicus Emergency services and led to multiple papers using SWOT 113 pass: Simoes-Sousa et al. (2025) and Laipelt et al. (2025). On the Farkadona event (Greece), a major flood event occurred during September 2023 and was the result of extreme rainfall in the area in early September. The event is related to the EMSR 692[2] of the Copernicus Emergency services. And on the Owensboro event (USA), a flood event occurred in February 2025 following a storm event that hit Kentucky.

2.3. SWOT information

The SWOT information for the four studied flood events is summed up in Table 3. A difference is observed in the SWOT PIXC version C images where no reprocessing was performed. The C sub-versions correspond to some algorithm minor changes, and all the details about updates are available in the release note (SWOT, 2025). The new main version D is currently available; however, reprocessing of old SWOT data has not yet been completed. Only Owensboro is observed at VV polarization, but as the SWOT incidence angle is low, the polarization effect is meaningless. In Chinon, the SWOT image has been acquired close to the flood peak. On Farkadona, the SWOT image available was acquired a few days after the flood peak, hence during the flood recession.

[1] https://riskandrecovery.emergency.copernicus.eu/EMSN194/reporting/
[2] https://rapidmapping.emergency.copernicus.eu/EMSR692/reporting

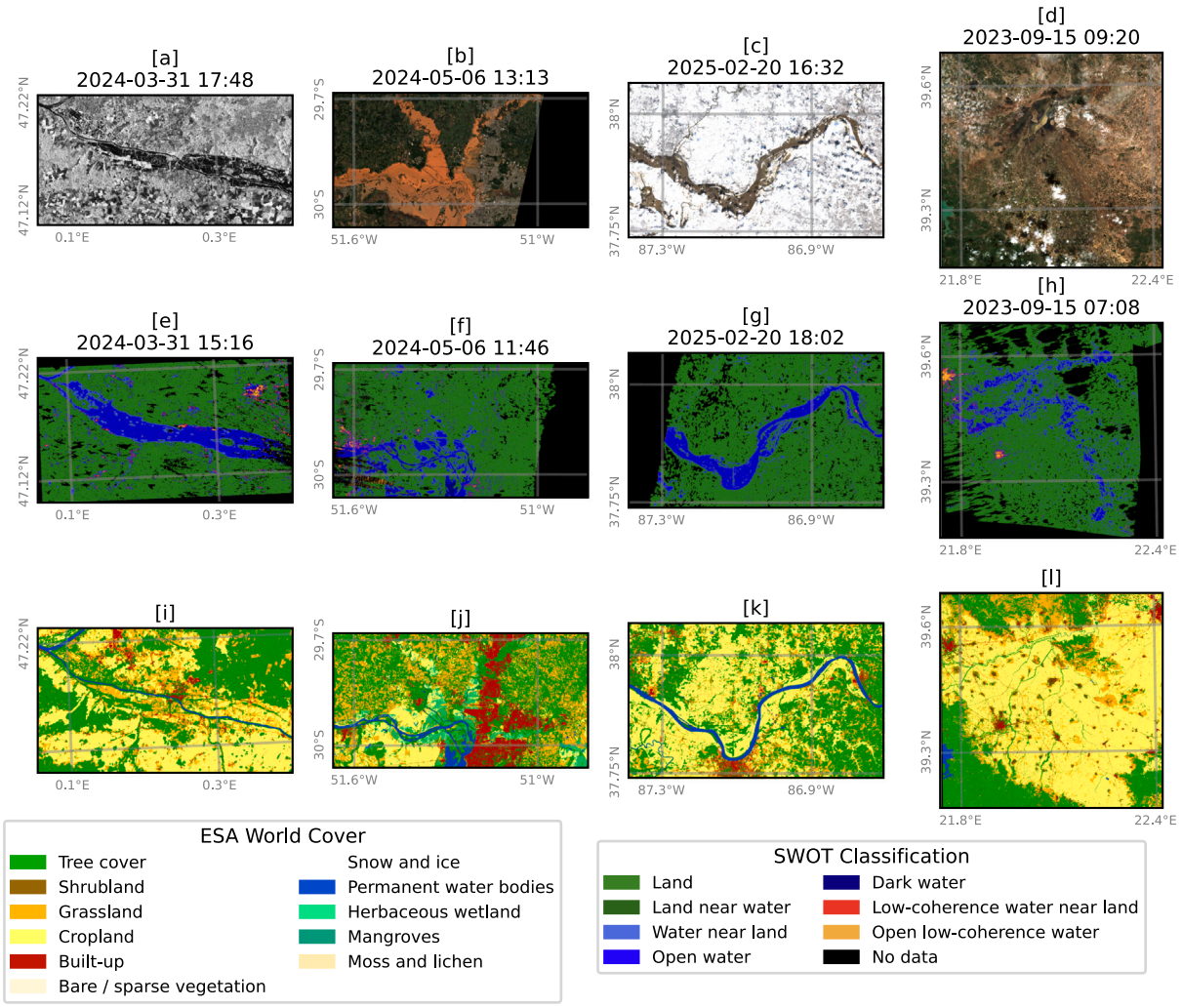

Fig. 1. Panel of Sentinel-1 and Sentinel-2 images used as comparison (first row), SWOT built-in classification (second row) and ESA WorldCover (third row) for each flood event. The flood sites are organized as: (a-e-i) Chinon, France; (b-f-j) Porto Alegre, Brazil; (c-g-k) Owensboro, USA; (d-h-l) Farkadona, Greece. (a) Sentinel-1 VV, and (b-c-d) Sentinel-2 True color images based on B4, B3 and B2 channels.

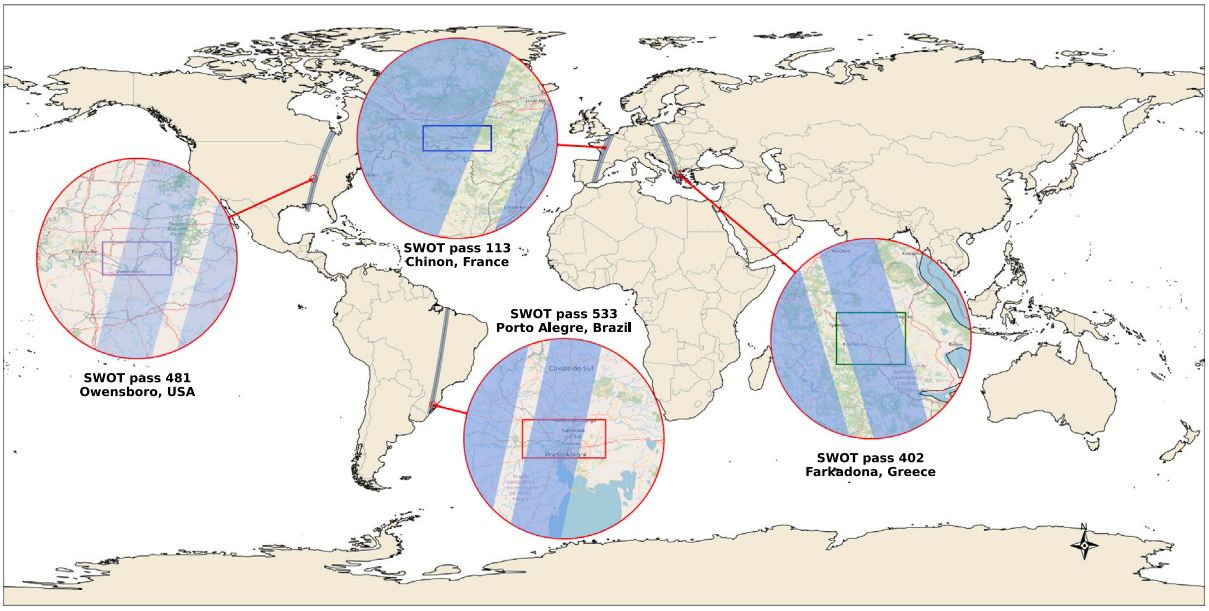

Fig. 2. SWOT pass and study sites localization.

Table 3
SWOT information for the four study cases.

Event	SWOT image date (UTC)	Studied passes	Selected tiles	Passes direction	Polarization	Other available passes	PIXC version
Chinon, France	2024-03-31 15:16	113	237L; 238L	Ascending	HH	320	PIC0_01
Porto Alegre, Brazil	2024-05-06 11:46	533	102R; 103R	Ascending	HH	492	PIC0_01
Owensboro, USA	2025-02-20 18:02	481	220L; 221L	Ascending	VV	466	PIC2_01
Farkadona, Greece	2023-09-15 07:08	402	085L; 086L	Descending	HH	417	PGC0_01

2.4. SWOT pixel cloud

In this study, we focus on the PIXC product (named L2_HR_PIXC) and on three radar variables: the backscattering coefficient (σ_0), the coherent power, and the interferometric coherence to understand their values and behavior during flood periods.

The backscattering coefficient (σ_0) represents the normalized radar return power from the Earth's surface, often expressed in decibels (dB). σ_0 quantifies the amount of the transmitted Ka-band radar signal that is scattered back toward the satellite by surface features, and is influenced by surface roughness, dielectric properties, and incidence angle. σ_0 is normalized by the illuminated ground area, locally tangent to an ellipsoidal model (Small, 2011). Near nadir, σ_0 is typically higher over smooth water bodies due to specular reflection and lower over rough surfaces or vegetated areas due to diffuse scattering. The backscattering coefficient is essential for detecting water bodies, assessing surface conditions, and supporting the interpretation of interferometric measurements by providing context on surface reflectivity. Boisot et al. (2015), Fatras et al. (2016), Fayne and Smith (2023), Fayne et al. (2024) studied Ka-band phenomenology on different types of soils, notably with the precursor experiment AirSWOT for the SWOT mission. They attempted to characterize the responses of Ka-Band over other types of soils and the impact of incidence angle and wind effects on small water bodies and diverse land covers. Those studies support the high sensitivity of SWOT responses to soil moisture, wind, and incidence angle.

The coherent power ($P_{coherent}$, also in dB) is computed from the rare interferogram and used in SWOT algorithms for water detection and water fraction estimation ((J.P.L. D-105504), 2023). Coherent power is sensitive to surface characteristics: it is higher over smooth, specular surfaces like calm water, and lower over rough surfaces or vegetated areas where scattering is more diffuse. It serves as an indicator of data quality for hydrologic and oceanographic elevation retrievals ((J.P.L. D-105504), 2023; (J.P.L. D-109532), 2024).

For SWOT, interferometric coherence (γ_{total}) near nadir quantifies the phase correlation between radar echoes received by the two satellite's Ka-band SAR antennas, which are mounted on both sides of a 10-m mast and operate in a single-pass, cross-track interferometric mode. This coherence is crucial for accurately retrieving WSE. Generally, coherence near nadir is elevated over calm, smooth water surfaces due to strong specular reflection, and it degrades over rougher water surfaces influenced by strong winds or waves, as well as vegetated floodplains. Since SWOT relies on Ka-band signals, which are sensitive to surface roughness and vegetation, small changes in surface conditions can significantly impact coherence. Compared with interferometry made with common SAR systems, SWOT illuminates the scene for two images used for the interferograms and coherence maps at the same time, thus canceling temporal decorrelation ((J.P.L. D-109532), 2024).

The interferometric coherence is the complex correlation coefficient between two Single Look Complex (SLC) images comprising the interferogram, defined as

$$\gamma_{total} = \frac{\langle s_1^* s_2 \rangle}{\sqrt{\langle |s_1|^2 \rangle \langle |s_2|^2 \rangle}} \tag{1}$$

where the angle brackets denote the statistical expectation, s_1 and s_2 the two complex SLC images, one per receiving antenna, and the asterisk, the complex conjugate: with this notation, $s_1^* s_2$ is the complex interferogram. The norm of the coherence, which varies between 0 and 1, directly links to the variance of the interferometric phase $\phi = \sphericalangle(s_1^* s_2)$. It can be highlighted with use of the Cramer–Rao bound asymptotic model to express the interferometric phase variance σ_ϕ^2 (Chen, 2023; Rodriguez and Martin, 1992).

$$\sigma_\phi^2 = \frac{1}{2}\left(\frac{1 - |\gamma_{total}|^2}{|\gamma_{total}|^2}\right)$$

where $|\gamma_{total}| = 0$ indicates that there is no correlation between the two SLCs and the interferometric values are random noise. On the contrary, if $|\gamma_{total}| = 1$ mean that the two SLCs are in total coherency and there is no noise in the data. Noticeably, the coherence over water bodies is found to be near 1, or at least significantly greater than the coherence over non-water surfaces.

Correlation sources in the context of across-track interferometry have been studied in the literature (Bohé et al., 2025; Bohé, 2023; Chen, 2023; Rodriguez and Martin, 1992; Rosen et al., 2000). The γ_{total} is linked to decorrelation sources and can also be written as:

$$\gamma_{total} = \gamma_{SNR}\gamma_{geom}\gamma_{ang}\gamma_{vol} \tag{2}$$

where γ_{SNR}, γ_{geom}, γ_{ang} and γ_{vol} are the noise, geometric, angular and volumetric correlation terms, respectively. Other small terms of decorrelation exist but are ignored here. γ_{geom} and γ_{ang} are instrument-related sources of decorrelation, and can be estimated from the knowledge of the instrument features and acquisition geometry. γ_{vol} is a surface-related source of decorrelation; it is used, in the Low-Rate acquisition mode (i.e. ocean mode) to estimate Significant Wave Height (Bohé et al., 2025). The last term, γ_{SNR}, is of prime interest for our study, and is given by:

$$\gamma_{SNR} = \left(1 + \frac{1}{SNR_1}\right)^{-1/2}\left(1 + \frac{1}{SNR_2}\right)^{-1/2} \tag{3}$$

$$SNR_a = \frac{P_a - P_a^{noise}}{P_a^{noise}} \tag{4}$$

where P_a the signal power and P_a^{noise} is the noise power for each channel $a \in [1, 2]$. According to the SWOT data, γ_{SNR} is the primary driver of total decorrelation (Peral and Esteban-Fernandez, 2018; Peral et al., 2024). It is important to note that SNR (hence γ_{SNR}) depends on the signal power, which is proportional to the local surface backscatter σ_0. Thus γ_{SNR} is modulated by the nature of the surface imaged in the pixel. A higher SNR generally enhances the effective contrast between land and water, as land brightness often falls below the thermal noise floor, thereby improving water detection (Lobry, 2017). To compute γ_{SNR}, we need SNR estimates for the two images s_1 and s_2.

P_a^{noise} is a 1D-vector given in the *noise* group of the PIXC file as a function of time (also referred to along-track index, or lines). The indexing between the noise indexes and the PIXC indexes is given in the SWOT Pixel Cloud Product description ((J.P.L. D-105504), 2023).

The SWOT PIXC includes a classification composed of seven classes described in Table 4. It results from an automated segmentation algorithm based on the coherent power of a pixel and its neighbors (Lobry, 2017). This classification gives information about the localization of water within the image. Two classes of water can be used as a water mask: the *open water* and *water near land* classes. Four SWOT classification maps for the flood events are available in Fig. 1 [e - f - g - h]. The water masks computed in the study are an addition of the classes

Table 4
SWOT classification table.

Class	Definition
1	Land
2	Land near water
3	Water near land
4	Open water
5	Dark water
6	Low-coherence water near land
7	Open-low-coherence water

Open water, *Water near land*, and *Dark water*. *Dark water* class is added to the mask to take into account areas with uncertainties. Cities can sometimes be classified as "open low-coherence water", this can be observed on Fig. 1 [h].

The classification algorithm takes into account multiple phenomenologies such as dark water, bright land pixels, and low-coherence water, among others. Multiple flagging algorithms are combined to compute the classification. The details of the phenomenology and algorithms are in the (J.P.L. D-109532) (2024) and (J.P.L. D-105504) (2023).

Water surfaces typically show higher backscatter than land at SWOT incidence angles. Still, certain conditions like smooth water surfaces can be too specular and cause dark water, where no signal is returned due to off-nadir reflection. Heavy rain can also cause similar signal loss. Dark water pixels are identified by the SWOT algorithm using Global Surface Water Occurrence (GSWO) dataset (Pekel et al., 2016) to flag such areas, which may lead to errors in regions with poor prior data, like floodplains. The GSWO map is thresholded using a dynamic threshold to achieve the best comparison with SWOT observations ((J.P.L. D-105504), 2023).

Similarly, bright land is flagged using a prior mask based on urban or developed areas. The low-coherence water flag identifies water regions with low phase coherence using a filtered, thresholded coherence measure. Additionally, specular ringing – artifacts from bright targets near nadir – are flagged across several quality metrics ((J.P.L. D-105504), 2023; (J.P.L. D-109532), 2024). In this study, affected low-coherence water pixels are discarded from the SWOT PIXC product to maintain data integrity.

2.5. Other external datasets

The ESA WorldCover (WC) dataset (Zanaga et al., 2022) is a global land cover classification dataset produced and distributed by ESA. It provides information about the Earth's surface, categorizing land into various classes such as forests, croplands, wetlands, urban areas, and more. It is designed to support environmental monitoring, climate change studies, and natural resource management. The ESA WorldCover dataset is freely accessible and available at a high spatial resolution (10 m). The dataset is based on Sentinel-1 and Sentinel-2 data (Zanaga et al., 2022), and the version used in this study was published in 2021, making it relatively recent and coherent with the observation scenes. The four ESA WC in the AOI are shown in Fig. 1 [i–j–k–l]. Most of the studied floodplains are composed of cropland or grassland. Chinon (Fig. 1 [i]) has numerous vegetation areas within its floodplains. Porto Alegre is a more complex AOI (Fig. 1 [j]). It is composed of urban areas, herbaceous wetlands, tree cover, crops, and grasslands. For Owensboro (Fig. 1 [k]), the floodplain is mainly composed of croplands with some tree cover. Urban areas are visible but are protected with dikes, as the river often floods the area. For Farkadona (Fig. 1 [l]), it is an area composed of a majority of cropland with some small villages or cities. The AOI does not contain a major river.

We generated a three-class mask based on the ESA WorldCover dataset to characterize land cover within the areas of interest. This mask facilitates the analysis of KaRIn signal responses in floodplains under different land cover conditions during flood events. The three classes correspond to forest, urban, and open areas. The forest class is defined by selecting pixels with a value of 10, representing the "Tree cover" class in the ESA WorldCover product. The urban class comprises pixels with a value of 50, corresponding to the "Urban" category within the study area. The open areas class includes all remaining ESA WorldCover classes, except for permanent water bodies, which are identified by a value of 80. Those water masks will be used in the analysis to compare the mean dry rasters with the flooded date rasters using histograms. Table 5 shows the percentages for each WC class and is consistent with the description of Fig. 1.

Table 5
WorldCover classes percentage within flooded areas. For each flood AOI defined, the percentage of pixels in each ESA WC group is represented.

	Chinon, France	Porto Alegre, Brazil	Owensboro, USA	Farkadona, Greece
Urban areas	0.36	0.37	0.25	2.82
Forest areas	6.75	6.32	1.39	8.12
Permanent water	1.38	3.11	0.14	3.80
Open areas	91.51	90.20	98.22	85.26

For this study, two different DEM datasets will be used. The first DEM dataset is the French RGE ALTI,[3] which is available at resolutions of 1 m and 5 m. The RGE ALTI is a gridded DTM designed to describe the French terrain relief. It is a high-quality DTM that covers the entire French territory and is therefore suitable for use in the case of the Chinon study site. The second dataset is FABDEM v1.2 (Forest And Buildings removed Copernicus DEM), which is a global elevation map at 30 m resolution that removes biases in building and tree heights from the Copernicus GLO 30 DEM (Hawker et al., 2022). It is currently the only DEM dedicated to flood monitoring available at a global scale and therefore, is used for the three other flood events. RGE ALTI 5m-DEM was retained for the Chinon case, as it offers a better resolution within this AOI.

3. Method

In this study, our goal is to understand SWOT Pixel Cloud data for flood event analysis to integrate SWOT-based flood observations into DA systems built on top of hydrodynamic models. In this article, we first attempt to examine the built-in SWOT PIXC classification method and analyze how and why it responds in different flood cases. In the second part of the article, three SWOT variables will be studied to compute the flood mask from them. The flood masks will then be compared with the reference images and the SWOT PIXC built-in classification to determine the pros and cons of each method.

The diagram of Fig. 4 exposes the method steps. The four selected AOIs are placed in different parts of the globe and in various configurations, which we have attempted to categorize considering world coverage within the AOIs before analyzing the images. To compare the SWOT PIXC with other data, a rasterization is performed, defined in Section 3.1. The reference flood mask data is processed with the FloodML algorithm (Section 3.2) from Sentinel-1 or Sentinel-2 images. Since Sentinel-1 and Sentinel-2 do not provide a perfect input for ground truth generation, we defined an *a priori* flood extent from the DEMs databases, which will be further referred to as the "manually-delineated" flood mask in this study (Section 3.2). To understand SWOT measurements during a flood event in a specific AOI, a dry reference of each analyzed variable was first needed. A dry mean raster of SWOT measurements is computed to both compare and detect changes within AOIs during the flood event (Section 3.3). From there, SWOT measurements can be better used to generate flood masks (Section 3.4) and compared visually or with scores to the other masks (Section 3.5).

[3] https://geoservices.ign.fr/rgealti

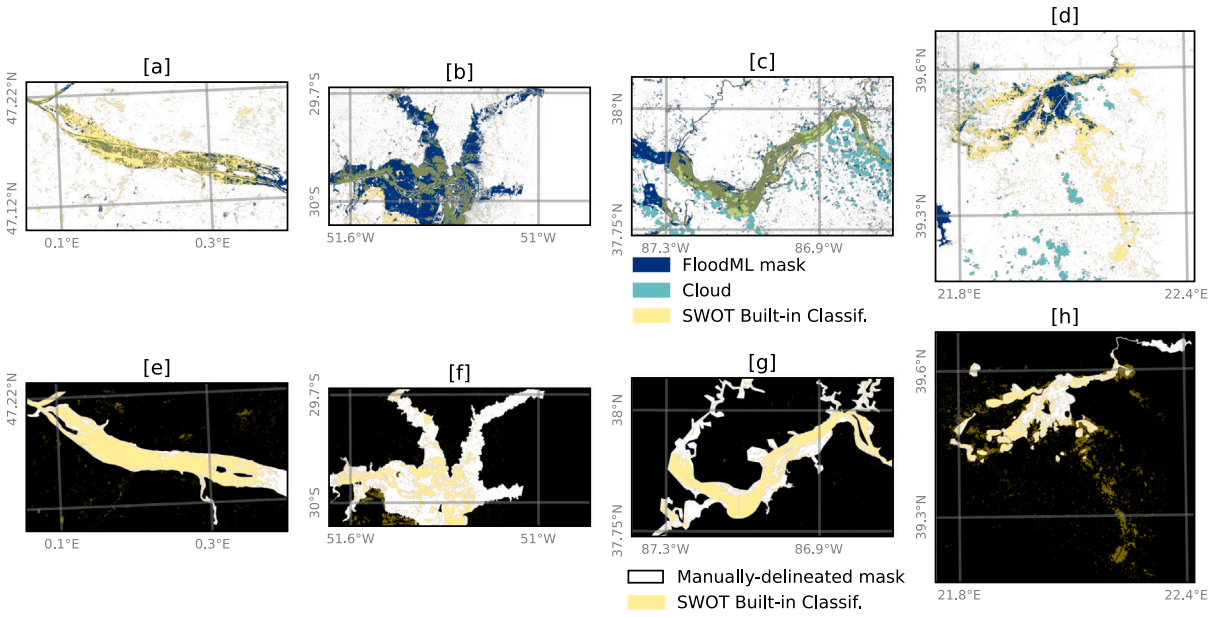

Fig. 3. FloodML water mask of Sentinel-1 and Sentinel-2 images (first row) and manually-delineated flood masks (second row) within the area of interest for study sites superposed with the SWOT built-in classification water mask. The flood sites are organized as: (a–e) Chinon, France; (b–f) Porto Alegre, Brazil; (c–g) Owensboro, USA; (d–h) Farkadona, Greece. FloodML images are organized as: (a) Cleaned FloodML mask from Sentinel-2 (2024-05-06 13:31 UTC); (b) Thresholded mask from Sentinel-2 (2025-02-20 16:32 UTC); (c) Thresholded mask from Sentinel-2 (2025-02-20 16:32 UTC); (d) FloodML mask from Sentinel-2 (2023-09-15 09:20 UTC). SWOT built-in classifications correspond to the flood date data.

3.1. Rasterization of SWOT PIXC

To compare multiple SWOT images and facilitate spatial comparisons, SWOT PIXC products are rasterized into approximately 10×10m grids within AOIs. The rasters are projected using the local Universal Transverse Mercator (UTM) zones and the WGS84 horizontal datum. SWOT L2_HR_Raster products are not used in this study as their resolutions (100 or 250 m) are considered too coarse for precise flood delineation. The rasterization process may smooth some noise of the pixel cloud by averaging multiple points for one raster pixel in certain areas. Rasterization is performed using the inverse distance to a power method with the nearest neighbor searching algorithm of GDAL. As mentioned earlier, pixels classified as low-coherent water and flagged with the specular ringing flag are discarded in this process. During this process, interferometric coherence and SNR coherence are computed. Auxiliary data are resampled with GDAL in the exact pixel resolution within AOI for better comparison.

3.2. FloodML and manually-delineated masks

Flood extent across the four study sites was mapped using a combined approach involving the FloodML algorithm and manual refinement based on topographic data. FloodML, a Random Forest-based classifier, detects flooded areas using Sentinel-1 (VV/VH), Sentinel-2, Landsat 8/9, and TerraSAR-X imagery, supported by DEMs (MERIT or COPDEM GLO-30) and ESA WorldCover. Trained on Copernicus EMSR cases using high-confidence water samples from the GSWO dataset (Pekel et al., 2016), it produces binary flood masks within minutes (Nguyen et al., 2022b). It achieves an overall accuracy of 86.86 % when validated across five test sites worldwide (Kettig et al., 2021). In this study, other types of classifiers were not tested.

While efficient, FloodML has known limitations in urban areas, forested floodplains, and snow-covered regions. For example, in Chinon (Fig. 3 [a]), Sentinel-1 missed vegetated flood zones; in Porto Alegre (Fig. 3 [b]), Sentinel-2 allowed clear detection of urban flooding; and in Ohio (Fig. 3 [b]), snow misclassification required a blue-band threshold correction (Bertels et al., 2016). Farkadona (Fig. 3 [b]) showed visible flood traces despite limited coverage.

To improve accuracy, manual delineation was performed using FloodML outputs in combination with a Height Above Nearest Drainage (HAND), derived from FABDEM (30 m resolution - Nobre et al. (2011)) or RGE ALTI DEMs (5 m resolution). FABDEM is used outside of Chinon flood case as it is the most accurate option available globally (Nandam and Patel, 2024; Meadows et al., 2024; Marsh et al., 2023). Comparing the theoretical flood extent from HANDs with FloodML results and SWOT classification enabled correction of misclassified areas due to DEM artifacts or EO limitations. The resulting flood maps provide more complete coverage, especially in areas obscured by vegetation or urban structures.

In sites like Chinon and Ohio (Fig. 3 [e] and [g]), uncertain flood boundaries were retained as potential flood zones for further analysis. While some uncertainty remains at the margins, HAND consistency supports the plausibility of these extents, making them suitable for validating other flood detection products, including those derived from SWOT.

The FloodML and manually delineated masks will later serve as references for comparing SWOT-derived masks generated using a simple histogram threshold. The manually delineated mask will also define the AOI for the histogram analysis.

3.3. Mean computation for dry control

The use of a non-flood witness is key to comparing the SWOT PIXC data acquired during a flood event with the expected values in a dry case. The mean of multiple dry dates has been computed for the three variables studied. We have selected four dry dates for each case within the range of available SWOT scientific orbit data (i.e., from 2023-07-21 onward) with the same pass (same incidence angles) as the flood event. The selected dates are SWOT images that correspond to a normal hydrologic regime with no significant errors (specular ringing, dark water...) in the SWOT data. The first five rows of Table 6 represent the flood event dates and the four selected dry dates are colored depending on the year period. Apart from the Porto Alegre flood event, the selected dry dates differ in the year period. This means that there may be changes in the radar signal responses

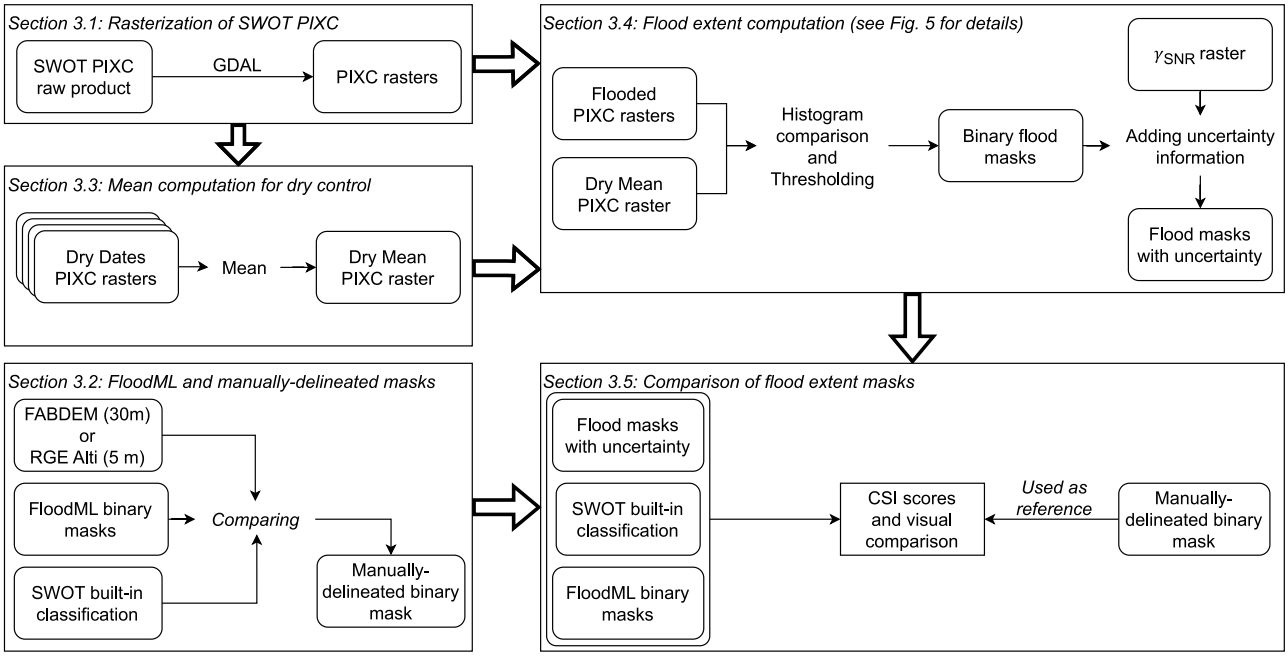

Fig. 4. Schematic of method processes divided by Section of the paper for the flood extent computation.

Table 6
Representation of SWOT selected dry dates for dry mean and general observation on SWOT images for the flood event date. December, January, and February (DJF) period is represented with blue text color, March, April, and May (MAM) with green text color, June, July, and August (JJA) with yellow text color, September, October, and November (SON) with orange text color. The last five rows contain information about the flood date images.

	Chinon, France	Porto Alegre, Brazil	Owensboro, USA	Farkadona, Greece
SWOT flood date	2024-03-31	2024-05-06	2025-02-20	2023-09-15
SWOT selected dry dates	2024-08-03 2024-08-24 2024-09-14 2024-10-05	2024-03-25 2024-04-15 2025-03-15 2025-04-05	2023-09-18 2023-10-29 2023-12-10 2024-03-23	2024-04-10 2024-05-01 2024-07-03 2024-07-24
Flooded vegetated areas	✓	✓	✓	
Flooded urban areas		✓		✓
Soil moistures			✓ (snow)	✓ (flood recession)
Specular ringing	✓	✓		
Dark water		✓		✓

due to differences in soil moisture, the vegetated states of tree covers, or croplands. In Owensboro, a snow signal may be observed on the mean raster as some dates are close to the snow period. The differences between the dry mean and the flood event for each case will be taken into account to enhance signal comprehension.

Also in the last part of Table 6, general observations and phenomenology observed on the flood event images are exposed. Those phenomena (specular ringing and dark water) and soil moisture will impact the SWOT image quality for flood extent retrieval. For the soil moisture cases (Farkadona and Owensboro), Sentinel-2 does not seem to detect any water where the SWOT signal is high. It can indicate a high soil moisture, as SWOT is sensitive to soil moisture.

3.4. Flood extent computation

The first step in defining the dry/wet flood extent is applied across the global Area of Interest (AOI) and separately for each SWOT variable: γ_{total}, σ_0, and $P_{coherent}$. This corresponds to Step 1 in the schematic (Fig. 5). The flood extent is derived by applying thresholds to the histogram of each ESA WorldCover (WC) class, as defined in Section 2.5. Each SWOT variable therefore, has two or three threshold values, depending on whether urban areas are included in the flood analysis.

Thresholds are manually determined by comparing histograms of mean dry rasters and flooded rasters within the floodplain for each WC class. For example, the threshold values for γ_{total} are presented in Section 4.5. Thresholds are selected where the flooded histogram is most prominent relative to the dry histogram.

In the second step (see Fig. 5), uncertainty classes are introduced within the manually-delineated flood extent (Section 3.2). This step uses a threshold on the signal-to-noise ratio, γ_{SNR}, to exclude areas where the radar signal is too noisy. Areas with $\gamma_{SNR} \geq 0.5$ are retained in the mask, while areas with low γ_{SNR} are assigned to a gray "low SNR" class, indicating insufficient signal quality for confident interpretation. These should not be considered flooded.

Only for γ_{total}, the third step (Fig. 5 Step 3) is performed on the remaining signal. This is to be consistent with the SWOT classification process, where the interferometric coherence is used to detect dark water areas. A second threshold is applied to detect "potential dark water"—areas that may be water-covered but are not captured in the signal. They are not always detected by the built-in classification,

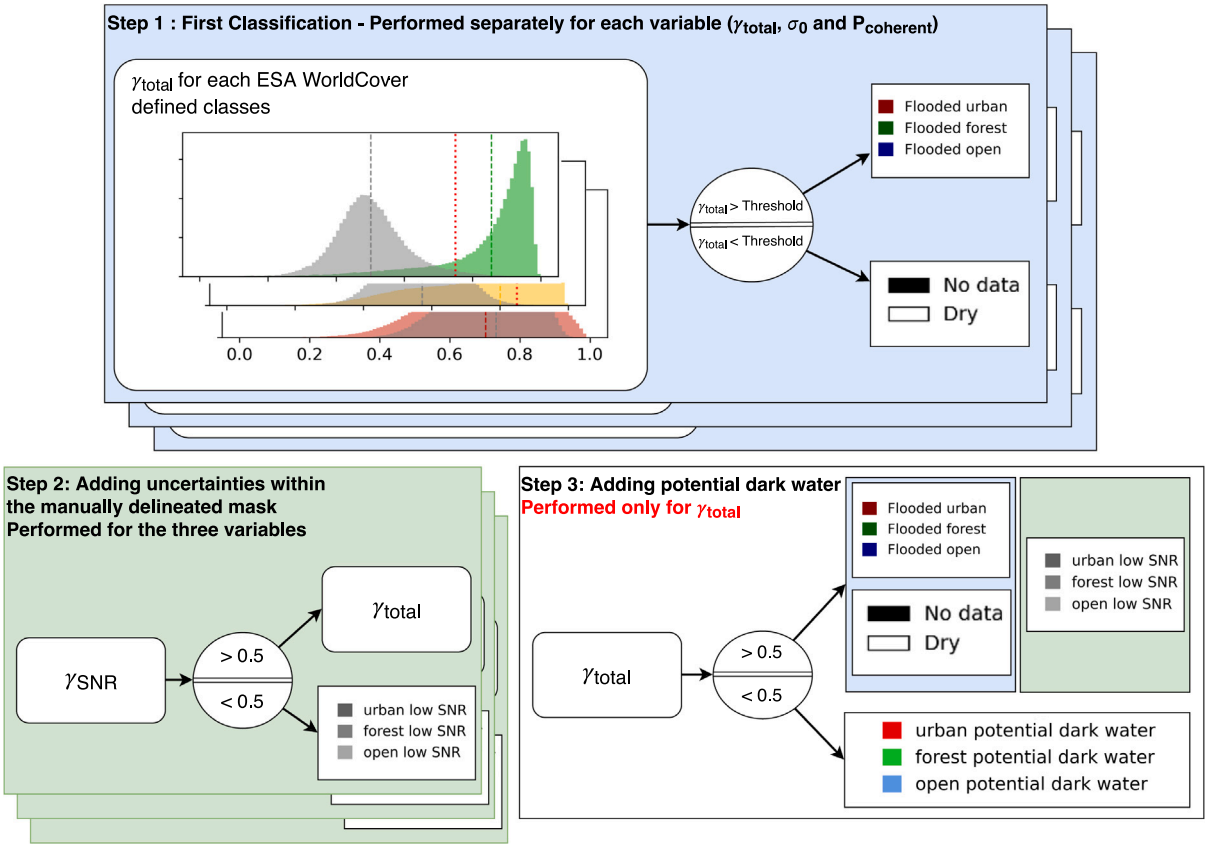

Fig. 5. Schematic of the masks computation process. Step 1 defines flooded and dry areas, while Steps 2 and 3 add regions of uncertainty to the masks. The color classes shown at the end of each step correspond to the legend used in Fig. 11, Fig. A 5 and Fig. B 5.

possibly due to inaccuracies in the GSWO *a priori* dataset. This class, like the dark water category in SWOT's built-in classification, is of low confidence and should generally be discarded unless used with caution.

If none of the thresholds in Steps 2 or 3 are met, the classification defaults to the decision made in Step 1 (i.e., Flooded or Dry).

3.5. Comparison of flood extent masks

Once the water masks are computed, a score comparison is performed between the γ_{total} water masks and the manually-delineated water masks (see Section 3.2). A Critical Success Index (CSI or Jaccard Index) is also computed within the manually-delineated mask to measure the similarity between the two masks. The CSI evaluation considers the FloodML flood extent maps as the reference flood maps. For γ_{total} masks, only flooded and potential dark water pixels are kept as wet pixels and are converted into binary data (wet/dry data). The CSI is also computed between the SWOT built-in classification, FloodML, and the manually-delineated mask to measure similarities between the three masks. For the SWOT built-in classification, all the pixels defined as non-land class (class index > 2, cf. Table 4) are used. This is to match the use of the low-confidence pixels kept in our masks. The CSI is computed using a contingency map with:

$$CSI = \frac{True\ Positive}{True\ Positive + False\ Positive + False\ Negative} \quad (5)$$

where *True Positive* is the number of pixels that are defined as wet by both rasters. *False Positive* is the number of pixels defined as wet by the SWOT mask (or FloodML mask) but defined as dry by the manually-delineated mask. On the contrary, *False Negative* is the number of pixels defined as dry by SWOT (or FloodML mask) but as wet by the manually-delineated mask.

Sentinel-1 and Sentinel-2 can be erroneous and can contain misclassification. That is why a visual comparison is performed, to check if SWOT complements the data, and if we can understand certain phenomena by visually comparing Sentinel-1 and Sentinel-2 with SWOT. The CSI is used more as a similarity score than a search for the perfect match between SWOT variables and the manually-delineated masks. The closer to 100, the better, keeping in mind that SWOT KaRIn is a new sensor with new signal physics.

4. Results

4.1. Comparison with the SWOT classification

The SWOT classification from the PIXC product, shown in Fig. 1, offers valuable information for flood analysis. Visual comparisons between Sentinel-1 and Sentinel-2 images and their FloodML masks (Fig. 3) – all acquired within 2.5 h of the SWOT data – highlight similarities and differences across flood events.

For Chinon (Fig. 3 [a]), SWOT's classified water pixels (open water and water near land classes) align well with Sentinel-1 observations, particularly detecting more flooded pixels in tree-covered northwestern flood areas. Owensboro (Fig. 3 [b]) also shows strong agreement with Sentinel-2, despite extensive snow cover which does not appear to affect SWOT detection.

In contrast, Porto Alegre (Fig. 3 [c]) and Farkadona (Fig. 3 [d]) show notable discrepancies with Sentinel-2 observations. Porto Alegre's classification misses significant flood areas in the north and center, partly due to a specular ringing artifact in the southwest. This image's low quality may relate to environmental factors on the acquisition

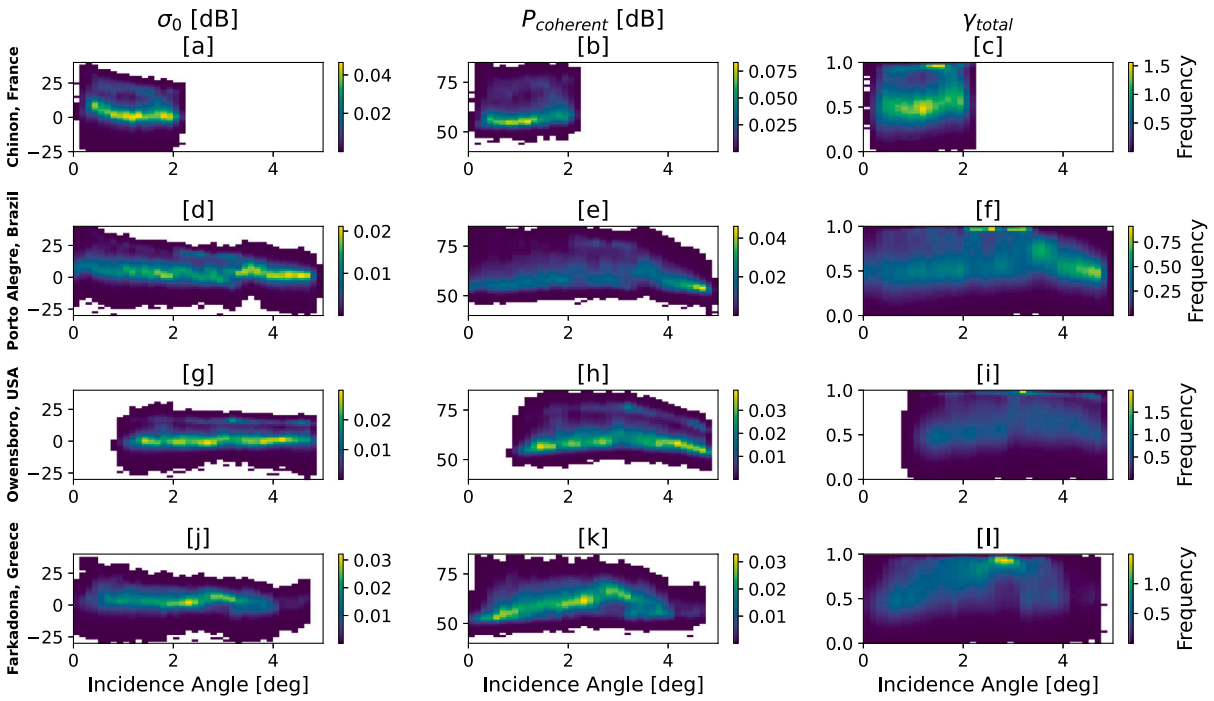

Fig. 6. Two-dimensional histograms showing the distribution of σ_0 (first column), $P_{coherent}$ (second column) and γ_{total} (third column) as functions of the incidence angle for the flood dates. The color intensity represents the frequency of data points within each bin. The flood sites are organized as: (a-b-c) Chinon, France; (d-e-f) Porto Alegre, Brazil; (g-h-i) Owensboro, USA; (j–k–l) Farkadona, Greece. Frequency values lower than 10^{-5} are discarded and set to white for visibility purpose.

date, including a northeast wind (~5.5 m/s) causing increased Ka-band signal scattering (Fayne and Smith, 2023) and a high water slope (~9.6 cm/km) in the main river (Laipelt et al., 2025), along with the attenuation effect of higher incidence angles (Fatras et al., 2016). Farkadona's rain-induced flood, captured during flood recession on cropland, shows an extended flooded area in SWOT likely influenced by soil moisture sensitivity (Fatras et al., 2016), explaining the broader extent relative to Sentinel-2.

These differences motivated further evaluation of SWOT interferometric variables to enhance classification. A deeper understanding of KaRIn's instrument response across various soil and land cover types is essential for improved flood event interpretation.

4.2. Incidence angle analysis

The two-dimensional histograms presented in Fig. 6 illustrate the evolution of σ_0, $P_{coherent}$, and γ_{total} as functions of the incidence angle on the respective flood dates. In all cases, except for the Farkadona event, a distinct flood-related peak is observed, which exceeds the primary (non-flood) signal peak. For γ_{total}, these flood peaks are concentrated near a value of 1.

Significant variations in signal response are observed at both low (< 1°) and high (> 2.5°) incidence angles. For σ_0 (Fig. 6 [a–d–g–j]), elevated signal values are seen at low incidence angles, particularly pronounced during the Chinon flood event (Fig. 6 [a]). The $P_{coherent}$ variable (Fig. 6 [b–e–h–k]) exhibits a clear curvature in response to the incidence angle, with a marked decrease in coherence beyond approximately 3°. For γ_{total} (Fig. 6 [c–f–i–l]), the signal also varies with incidence angle, though the distribution appears more diffuse compared to the other two variables.

No distinct flood-related peak is observed in the Farkadona case (Fig. 6 [j–k–l]). This can be attributed to the fact that the SWOT acquisition occurred during the flood recession phase, and the region lacks a major river system. Nonetheless, elevated signal values may still reflect increased soil moisture resulting from the preceding flood event.

These results suggest that σ_0 and $P_{coherent}$ are more sensitive to changes in incidence angle, particularly near their threshold values, which could significantly influence flood detection performance. In contrast, γ_{total} demonstrates a more stable response, with flood-related values clustering near the upper limit of the variable range.

4.3. Dry mean raster computation

Direct comparison between non-flooded and flooded SWOT PIXC observations is impeded by the application of buffer masks that remove pixels distant from water bodies, resulting in no-data gaps on dry dates and complicating temporal analyses. To address this, a temporal dry mean was computed from four SWOT acquisitions on the same satellite pass as each flood event. This approach partially fills no-data regions and enables more consistent comparison with flood observations.

As shown in Fig. 7, histograms of interferometric coherence derived from the dry means exhibit near-Gaussian distributions with means around 0.5–0.55, while distinct peaks near 0.95 in the Porto Alegre and Owensboro events (Fig. 7 [b,c]) indicate strong river signatures. Similar peaks are observed for coherent power and σ_0 in Figure A 2 and B 2, with water-related maxima around 75–80 dB and 18–20 dB, respectively, clearly distinguishable from dry soil. Areas without pixels on a dry date can be filled with data from another dry date during the mean computation, which explains the higher magnitude of the mean raster.

Maps of the dry mean rasters (Fig. 8; Fig. A 3 and B 3) reveal the incidence angle impact on σ_0 and $P_{coherent}$, and residual masked areas, notably in floodplains such as Chinon. Selecting appropriate dry dates proved especially challenging in agricultural areas like Farkadona, where narrow channels dominate, complicating flood-to-dry comparisons. Vegetation dynamics also introduce variability in the dry means, particularly for Chinon and Farkadona, as detailed in Section 3.3. Urban areas and roads consistently appear as bright land but may be excluded from analysis where known flooding occurred (e.g., Porto Alegre, Farkadona).

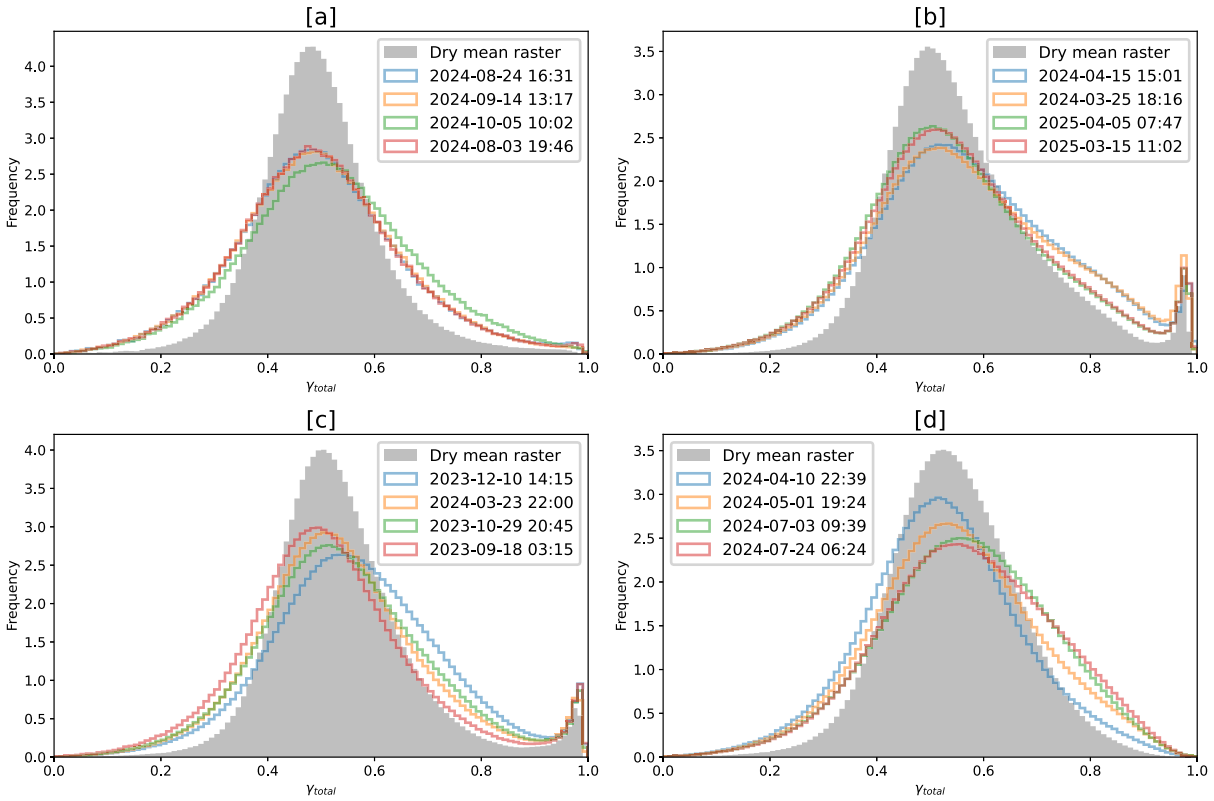

Fig. 7. Histograms of γ_{total} dry rasters within the floodplains and the mean dry raster. (a) Chinon, France, (b) Porto Alegre, Brazil, (c) Owensboro, USA, (d) Farkadona, Greece.

For Porto Alegre, the dry mean spans images from March–April 2024 and 2025, capturing a mix of partially flooded and dry crop-grass conditions, explaining the observed brightness in Fig. 8 [b]. In Owensboro, the mean includes winter 2023 and early spring images, potentially influenced by snow cover and melt, with bright signals visible in Fig. 8 [c] (rectangles B and B'). However, σ_0 maps in this case appear less sensitive to soil moisture than $P_{coherent}$ and γ_{total}, as the same features in the purple rectangles do not exhibit high backscatter.

4.4. Flooded variable maps

In this section, we present the interferometric coherence maps in Fig. 9 during the four flood events, which can be easily compared with the dry mean maps of the previous sections.

For Chinon (Fig. 9 [a]), the floodplain is obvious. On the A rectangle, a small river under the riverbank forest is distinguishable. This river is also visible on coherent power (Fig. A 1 [a]) and on σ_0 (Fig. B 1 [a]). However it is not distinguishable in the dry mean raster (see rectangle A Fig. 8 [a], Fig.A 3 [a] and B 3 [a]). More details are visible in the floodplains on the maps of $P_{coherent}$ and σ_0. However, the variables are more impacted by the incidence angle, making them less flat along the near range–far range axis. It is noted that the East part of those subplots is under SWOT nadir areas. It is impressive to detect part of the flood within these noisy areas impacted by specular ringing. It is an area where much uncertainty will remain in the data. In Owensboro (Fig. 9 [c]), the images display strong contrast due to the combined presence of snow cover and flooding. Despite this, the flood extent remains largely distinguishable (by visual inspection). Compared to Sentinel-2 imagery, the regions marked B and B' are more likely to correspond to areas with wet snow or water beneath the snow. However, for Porto Alegre (Fig. 9 [b]) or Farkadona (Fig. 9 [d]), compared to Sentinel-2 FloodML masks or even the direct images, it is clear that the flood extent is more complex to discriminate. The Porto Alegre signal is of poor quality, missing a significant amount of data compared to what could be expected theoretically, particularly in comparison to Sentinel-2. The SWOT image does not detect the flood in the northern part as clearly as it could be, and the main floodplain is composed of numerous low-coherence patches that could be interpreted as "dark water". The southeast part of the flood, visible on Sentinel-2, is also missing on the SWOT signal. For Farkadona, the soil moisture impacts KaRIn signal, compared to the Sentinel-2 FloodML mask, this image is brighter and might be unusable for a correct flood extent computation. This can be explained by the fact that it is an image taken during the flood recession. Similar observations can be made on the σ_0 and $P_{coherent}$ maps.

4.5. Histograms within flooded areas

As it is difficult to identify differences between the dry raster and the flood event pixel-wise without losing information on the flood extent, comparing histograms helps us define thresholds for the three variables and the WC filter. The Fig. 10 exposes γ_{total} histograms over each flood event (rows) and every WC filter (columns) within the floodmask defined on Section 3.2. Dry means histograms are bell-shaped on every WC filter. Compared to them, the flooded histograms are left-skewed with some specificity. In open areas, the water peak is found around 0.95 for γ_{total}. Fig. 10 [a] (Porto Alegre) histograms come with a second peak near 0.45. This is the result of the low coherence visible on the maps in the main floodplain and on part of the flooded northern areas. Globally, flooded forest area histograms are also left-skewed histograms, but with more dissimilarities. Farkadona forest (Fig. 10 [e]) and urban (Fig. 10 [f]) subplots, compared to the open areas, represent a small percentage of the global group of pixels and they should be interpreted with great care. Forest flooded peaks are above 0.8 and are still easily distinguishable from the dry mean histograms. A threshold method here might misclassify pixels as flooded. Only Porto Alegre and

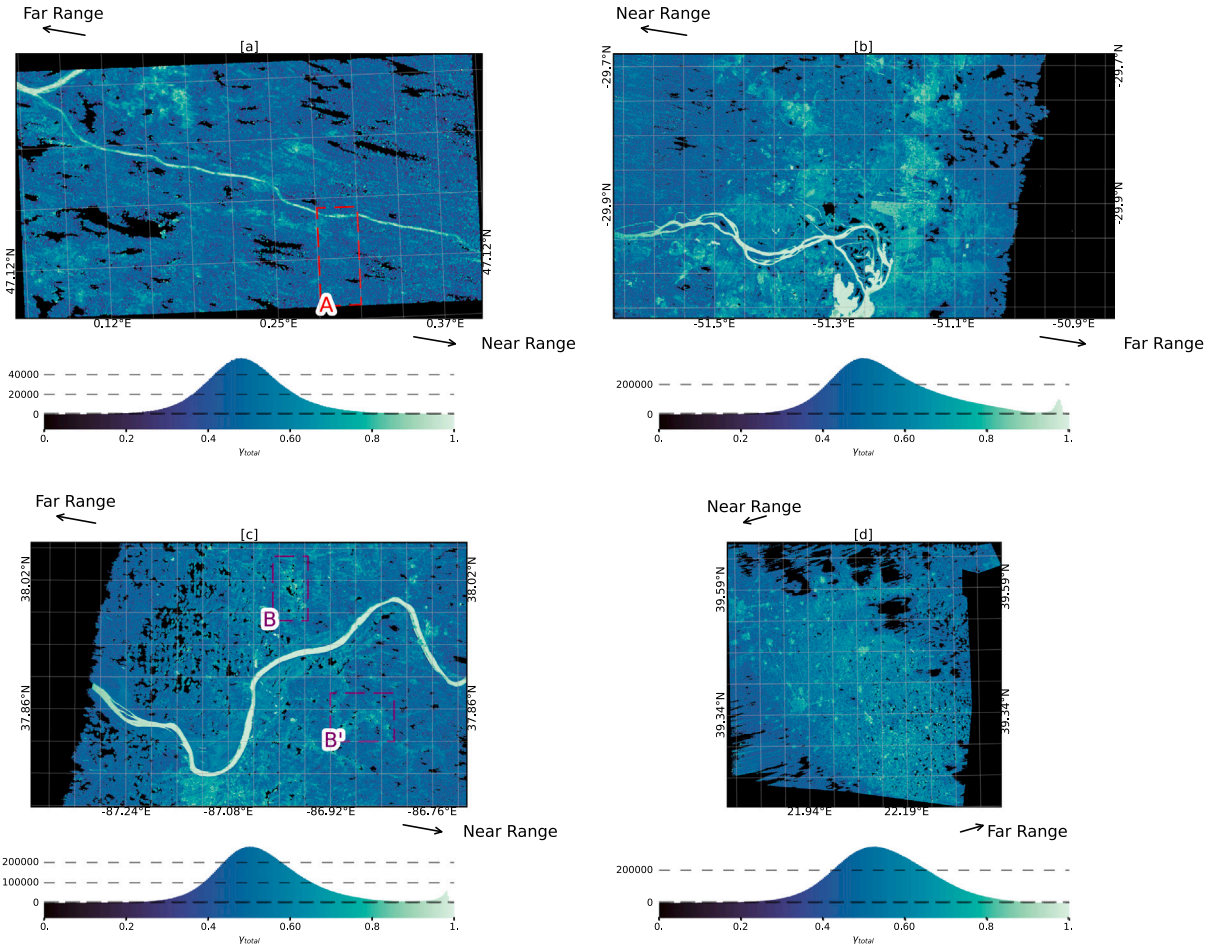

Fig. 8. Maps of the γ_{total} mean dry raster. (a) Chinon, France, (b) Porto Alegre, Brazil, (c) Owensboro, USA, (d) Farkadona, Greece. Black pixels are no-data pixels. Highlighted rectangles A, B and B' mark zones of interest for further exploration and analysis.

Farkadona histograms are presented for the urban filter. By analyzing the Chinon and Owensboro flood events, we determined that no urban areas were flooded and were therefore excluded from the analysis and thresholding. Farkadona-flooded urban areas (Fig. 10 [f]) have a specific signal compared to the dry mean, but it is difficult to threshold and draw a conclusion with this small number of pixels. A threshold is still set around the end of the dry mean histogram. Conversely, for Porto Alegre (Fig. 10 [c]), the dry mean and flooded histograms are similar. However, when performing a pixel-wise difference on urban potential flooded areas (using the manually-delineated flood mask defined), we observed a negative difference in the flooded regions compared to the unflooded ones. Therefore, we decided to apply the threshold on the pixel-wise difference for the urban filter on Porto Alegre.

$P_{coherent}$ and σ_0 histograms (Fig. A 4 and B 4) are more complex, but the water signal is still distinguishable. In both variables, the low values of Porto Alegre are not visible. The water peaks can be closer to the dry peaks, especially in the forest areas. In the coherent power, three peaks can be detected in both the open and forest filters in Owensboro (subplots [i] and [j]). Those peaks could be the result of the snow cover signals. In urban areas, no distinct signal was detected in relation to those variables.

As seen in Table 7, all thresholds are in the same range of values. Threshold values for $P_{coherent}$ and σ_0 can be found in Table A 1 and B 1. The direction of the threshold is described in the Table; for example, if the sign is ">" ("<"), then the left (right) part of the histogram is defined as wet. For Porto Alegre, we determined that it was easier to discriminate between flooded and non-flooded urban areas by using histograms of the pixel-by-pixel difference between the dry mean and the flooded date. This is not performed on $P_{coherent}$ and σ_0. Moreover, a lower signal was detected in flooded urban areas in Porto Alegre compared to the mean, explaining the left threshold and its low value. Nothing can clearly explain the signal's drop compared to the selected dry mean. The next step could be to detect the threshold value automatically, and if necessary, compare specific areas pixel-wise.

Table 7
γ_{total} threshold values used for SWOT flood masks. For urban areas in Porto Alegre, the threshold is performed on the histogram of the difference pixel by pixel between the dry mean and the flooded date.

	Open areas	Forest areas	Urban areas
Chinon, France	> 0.75	> 0.75	NaN
Owensboro, USA	> 0.85	> 0.7	NaN
Farkadona, Greece	> 0.85	> 0.85	> 0.9
Porto Alegre, Brazil	> 0.8	> 0.65	< - 0.1

4.6. Flood extent computation and comparison score

4.6.1. Flood extent computation

Fig. 11 presents flood extent maps derived from the γ_{total} thresholding method (Section 3.4), using WC-class-specific thresholds defined in Section 4.5 and Table 7. Permanent water bodies were excluded, and only floodplain areas were retained. In general, the resulting masks align well with both the built-in SWOT classification and FloodML products (Fig. 3).

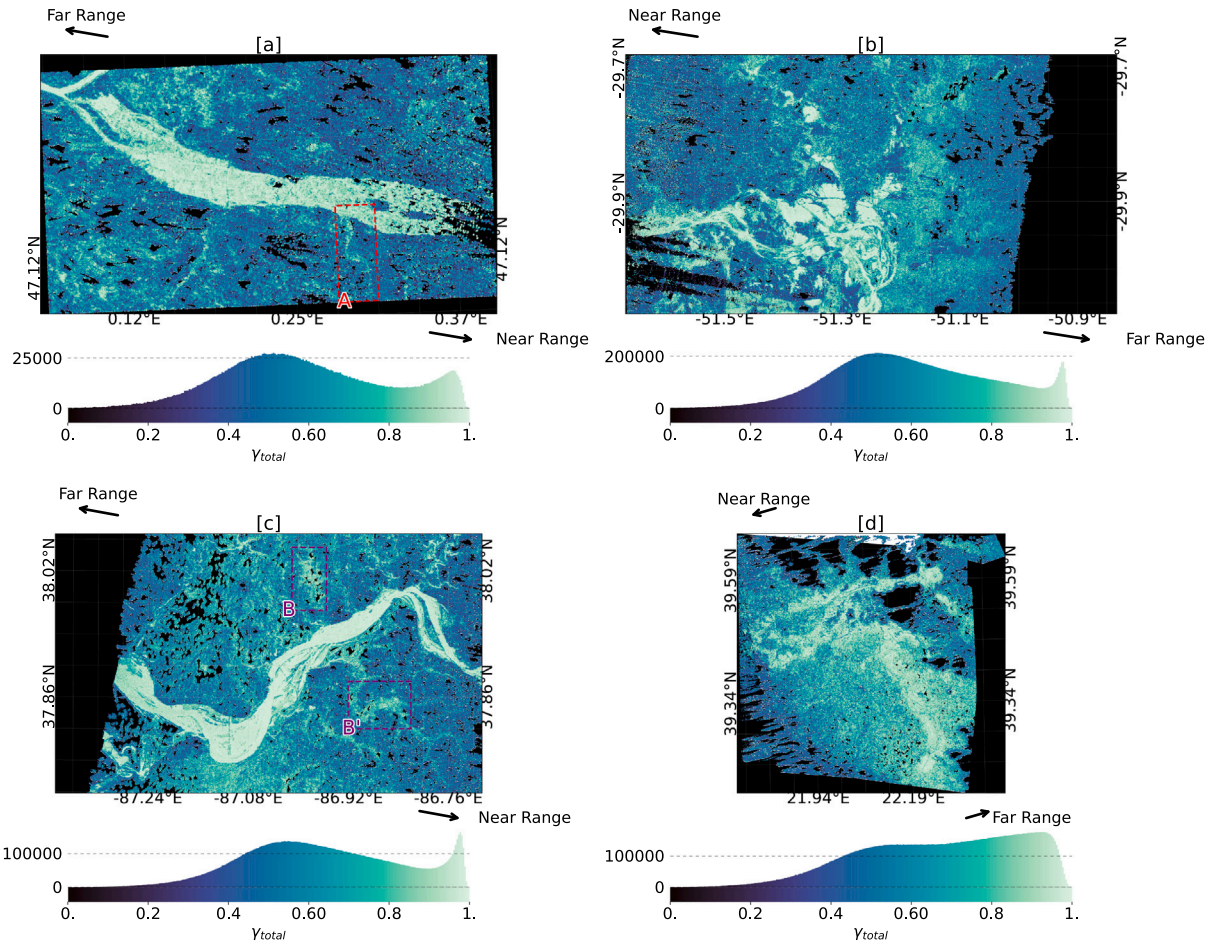

Fig. 9. SWOT interferometric coherence and its associated histogram within AOI. (a) Chinon, France, (b) Porto Alegre, Brazil, (c) Owensboro, USA, (d) Farkadona, Greece. Black pixels are no-data pixels. Highlighted rectangles A, B and B' mark zones of interest for further exploration and analysis.

Across all sites, SWOT detects both open water (dark blue) and inundated vegetated areas (dark green). However, isolated noisy detections are present outside floodplains, likely due to soil moisture variability, proximity to urban structures, or radar noise. Low SNR zones are especially evident in the far-range portions of the SWOT swath, particularly in the Porto Alegre (Fig. 11 [b]) and Owensboro (Fig. 11 [c]) cases, as well as in regions affected by specular ringing (e.g., southwest of Porto Alegre). Notably, low-SNR detections are also present in Farkadona (zoom [c]), despite clear flood evidence in the optical imagery.

In Chinon (Fig. 11 [a]), the rectangle A highlights a small river obscured by vegetation, more clearly detected using $P_{coherent}$ and σ_0 (Fig. A 5 [a] and B 5 [a]). Rain-formed ponds appear in the southwest, while bright patches in the northwest, near urban areas, may indicate signal contamination. σ_0 exhibits strong sensitivity to incidence angle, with forested regions in the near-range erroneously classified as wet. In contrast, $P_{coherent}$ shows reduced angular sensitivity and better delineation of the river in rectangle A, along with less background noise.

In Porto Alegre (Fig. 11 [b]), the γ_{total} mask offers improved delineation of flooded vegetation and urban zones (zooms [a] and [b]), corroborated by Sentinel-2 imagery. However, large low-coherence areas and low-SNR zones introduce uncertainty. σ_0 performs poorly near nadir due to incidence angle effects, while $P_{coherent}$ offers more balanced detection across the swath, albeit with lower sensitivity to flooded urban areas.

For Owensboro (Fig. 11 [c]), flood detection closely matches the built-in classification. Additional wet regions in rectangles B and B' may correspond to snowmelt or water under snow. This signal is weaker in σ_0 (Fig. B 5 [c]), which shows limited angular bias. Conversely, $P_{coherent}$ (Fig. A 5 [c]) is noisier and less responsive to small rivers, with performance affected by incidence angle and surface snow conditions.

In the Greece case (Fig. 11 [d]), flood detection is poor when compared to the FloodML reference. The region's high soil moisture and cropland dominance—alongside minimal tree cover—likely mask actual inundation. Urban signals are faintly visible in zoom [c]. Here, σ_0 (Fig. B 5 [d]) outperforms other variables due to reduced sensitivity to soil moisture, while $P_{coherent}$ (Fig. A 5 [d]) shows the strongest degradation.

4.6.2. CSI score comparison

Table 8 compares CSI scores in percentage between the different masks and the manually-delineated mask used as reference within the global AOI. Chinon and Farkadona are quite close to the classification's CSI compared with manually-delineated masks. $P_{coherent}$ and σ_0 CSI scores are quite similar to the γ_{total} scores. When the AOI contains, like in the Chinon event, a lot of tree cover, SWOT masks are better than FloodML. $P_{coherent}$ can be more effective in this case. However, γ_{total} masks give better scores when the images are of poor quality, such as in Porto Alegre, as the flooded masks account for low-coherent pixels. In this case, the FloodML mask remains better as the optical image is cloudless. On Owensboro or Farkadona, our masks and the classification CSIs are close to each other. In the first event, this is explained by the high snow cover that was filtered on FloodML and the impact of the incidence angle. Regarding the second one, this is the impact of high soil moisture, which reduces the SWOT mask quality.

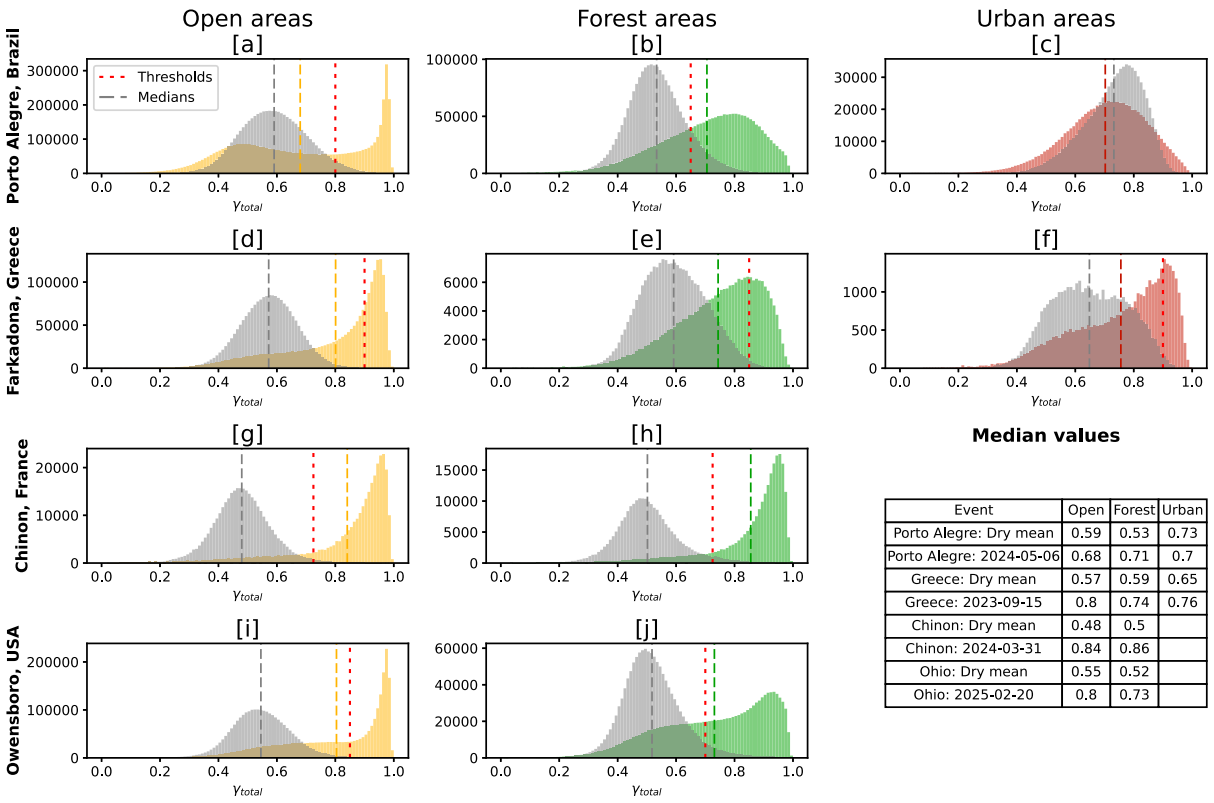

Event	Open	Forest	Urban
Porto Alegre: Dry mean	0.59	0.53	0.73
Porto Alegre: 2024-05-06	0.68	0.71	0.7
Greece: Dry mean	0.57	0.59	0.65
Greece: 2023-09-15	0.8	0.74	0.76
Chinon: Dry mean	0.48	0.5	
Chinon: 2024-03-31	0.84	0.86	
Ohio: Dry mean	0.55	0.52	
Ohio: 2025-02-20	0.8	0.73	

Fig. 10. Histograms of the interferometric coherence for each world cover filter within the floodplain. The flood sites are organized as : (a–b–c) Porto Alegre, Brazil, (d–e–f) Farkadona, Greece, (g–h) Chinon, France, (i–j) Owensboro, USA. The ESA filters are organized as : (a–d–g–i) Open areas, (b–e–h–j) Forest areas, (c–f) Urban areas. Grey histograms represent the dry mean raster, and the colored histograms represent the flood event. The vertical dashed lines represent the median values. If they appear, the vertical dotted red lines are the threshold values. The table exposes median values of each dry period and flood event histograms.

Table 8
CSI (%) within global AOI for the computed masks. The manually-delineated mask is taken as the reference in the CSI score computation.

	Chinon, France	Porto Alegre, Brazil	Owensboro, USA	Farkadona, Greece
γ_{total} mask x *Manually-delineated*	64.92	42.54	48.42	20.36
$P_{coherent}$ mask x *Manually-delineated*	69.98	29.38	47.57	24.51
σ_0 mask x *Manually-delineated*	62.64	28.22	48.95	26.61
Classification x *Manually-delineated*	59.55	22.95	40.14	24.44
FloodML x *Manually-delineated*	30.91	70.55	34.9	42.4

Globally, the three variable CSIs are close to each other, and depending on the event, it is better to take one or another.

4.6.3. Flood extent compared with manually-delineated and FloodML masks

In this section, general observations are made about a visual comparison with the FloodML flood mask (Fig. 12) and with the manually-delineated mask (Fig. 13) defined in Section 3.2. Coherent power (respectively σ_0) comparisons with FloodML masks or with the manually-delineated masks are found respectively in Figure A 6 (Fig. B 6) and Figure A 7 (Fig. B 7). The binary SWOT masks are a union of the flooded classes and the pseudo dark-water classes defined in the previous section. This visual comparison will help explain the observed CSI values more clearly.

If the vegetated areas are too dense, neither Sentinel-1 nor Sentinel-2 can see through them. However, when comparing the different masks and FloodML, SWOT detects water under tree covers in Chinon (subplots [a]), the northern part of Porto Alegre (zoom [a]), and areas near the southernmost meander of the Owensboro AOI. SWOT gives a more precise flood mask in those areas. Coherent power and σ_0 can better detect small structures, such as small rivers under trees, as seen in Chinon. But the two variables are sensitive to the incidence angle, which deteriorates flood masks, especially near the nadir. σ_0 mask seems more accurate for an analysis on high soil moisture areas (Fig. B 6 [c] and [d]).

Areas with low SNR are discarded for the binary mask, impacting the comparison of the results. In Porto Alegre (Fig. 12 [b]), the γ_{total} mask is close to FloodML, even without the low SNR. There is some overdetection in the southwest part where the specular ringing phenomenon occurred. In the zoom areas, FloodML from Sentinel-2 and γ_{total} mask detect both the flood in urban areas in the same areas. In the zoom area of Farkadona (Fig. 12 zoom [c]), it is noted that where FloodML detects water with Sentinel-2, SWOT does not see it. It is a combination of SWOT non-detection and low-SNR areas.

The same observations are made in the comparison with the manually-delineated mask. In Figure A 7, coherent power masks are compared with the manually-delineated mask. Compared to γ_{total} masks, the results are globally less accurate across the four subplots, with more noise, higher sensitivity to soil moisture, or to the incidence angle. However, it can detect smaller structures, such as those in rectangle A of subplot [a]. For σ_0 masks, as shown in Figure B 7, some

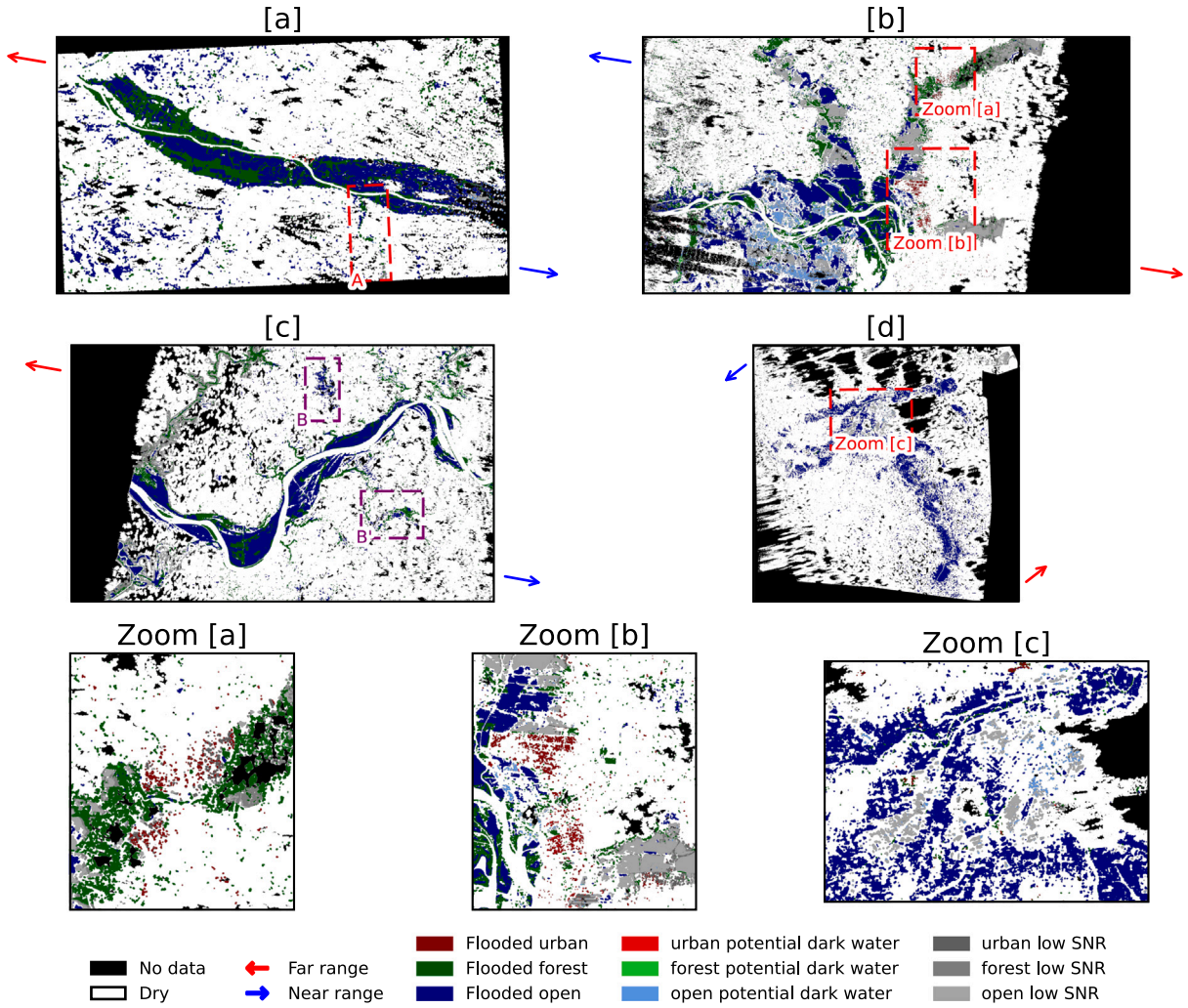

Fig. 11. γ_{total} **Flood extent computed from histograms within each world cover filter.** Black pixels represent the "no data" value and white pixels the non-flooded pixels. (a) Chinon, France, (b) Porto Alegre, Brazil, (c) Owensboro, USA, (d) Farkadona, Greece. (Zoom [a]) Porto Alegre, Brazil: Zoom in the north urban area; (Zoom [b]) Porto Alegre, Brazil: Zoom in the south urban area; (Zoom [c]) Farkadona, Greece: Zoomed-in view of Metamórfosi city and its neighborhood. Highlighted rectangles A, B and B' mark zones of interest for further exploration and analysis.

subplots exhibit high sensitivity to the incidence angle, as previously observed (subplots [a] and [b]). However, in some cases, the masks seem more accurate, like in the Farkadona flood case (subplot [d]) or in Owensboro, where soil moisture impacts less variable signals.

A merge of the three masks was tested by doing the intersection of the three masks. This has the merit of reducing the small areas detected as water outside the floodplains. However, it also removes the valuable information that some variables were able to detect within the floodplain that others could not. This is the case for Porto Alegre, for example, where the urban areas detected as flooded in the interferometric coherence were removed during the merge, as σ_0 and $P_{coherent}$ were unable to detect those areas. A method for better mask fusion could be investigated in future work.

5. Discussion

In the context of flood study and flood extent extraction, the built-in classification from SWOT PIXC is accurate in most cases. A PIXC product without any big limitations (from dark water, wind effect, soil moisture...) yields a high-quality flood classification, as observed for the Chinon flood event. It can also be correct in some problematic cases, for instance, with snow cover (as seen in the Owensboro event). SWOT can detect floods under tree cover and dense vegetation. This is confirmed in the three flood events with large tree cover areas, specifically the Chinon, Porto Alegre, and Owensboro cases. The results exceed expectations, with even small rivers under vegetation, including those less than 10 m wide, being visible using either σ_0 or $P_{coherent}$ in areas like Chinon and Owensboro. However, this result is not straightforward when using Ka-band. Over open areas, neither the classification nor our methodology is accurate when the soil moisture is high. This is illustrated in the Farkadona case, where the SWOT-based flood masks contain overdetected areas compared to the Sentinel-2 FloodML binary mask. This is observed quantitatively (with the CSI) but also qualitatively on the figures of Sections 4.6.2 and 4.6.3. Low coherence and dark water data detection are also a problem. This is primarily due to the built-in classification algorithm, which utilizes the GSWO database to detect dark water, as well as missing large flooded areas in some cases. This is illustrated by the Porto Alegre event, where the SWOT products missed many low-coherence areas with good SNR in the built-in classification.

The built-in classification and the binary flagging provided in the PIXC were thus used to identify areas with specular ringing and other complex features. A group of PIXC pixels that may contain useful information but should be interpreted with caution are those located near nadir, directly beneath the SWOT baseline, as these can be affected by reduced measurement accuracy. However, it is essential to

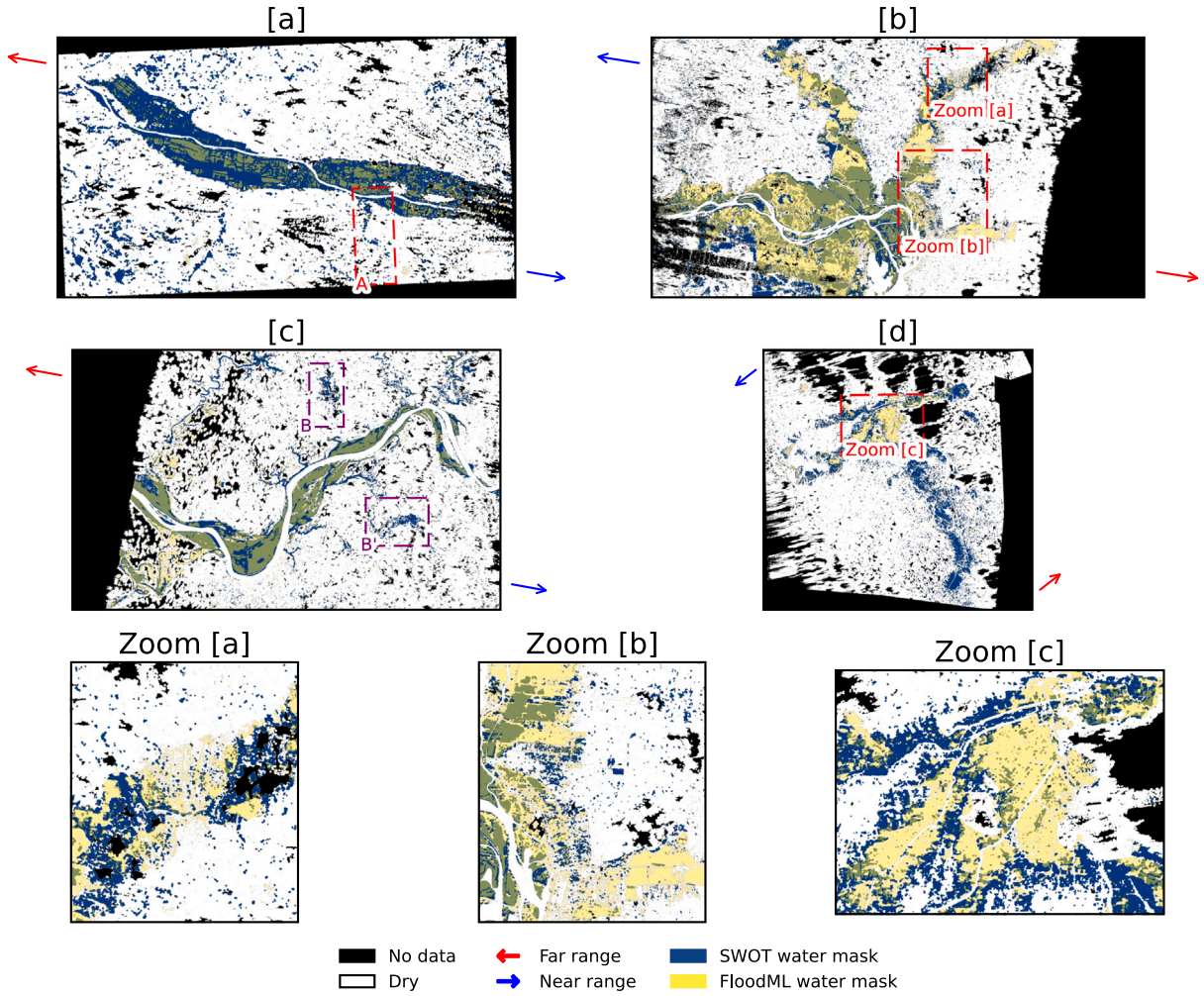

Fig. 12. Visual comparison of γ_{total} and FloodML water mask. Black pixels represent the "no data" value and white pixels the non-flooded pixels. (a) Chinon, France, (b) Porto Alegre, Brazil, (c) Owensboro, USA, (d) Farkadona, Greece. (Zoom [a]) Porto Alegre, Brazil: Zoom in the north urban area; (Zoom [b]) Porto Alegre, Brazil: Zoom in the south urban area; (Zoom [c]) Farkadona, Greece: Zoomed-in view of Metamórfosi city and its neighborhood. Highlighted rectangles A, B and B' mark zones of interest for further exploration and analysis.

examine the binary quality flag of the PIXC files and remove the data if necessary. This is also the case for our analyzed events, where pixels with a specular ringing flag and low coherence values were excluded from PIXC. The other data with the specular ringing flag is kept but viewed with great caution. Several undetected areas in the built-in classification were also classified as low-SNR or low-coherent water, as indicated by the study of γ_{total}, which is more informative. The study of γ_{total} on Porto Alegre showed that the histogram can be challenging to analyze. Some peaks can appear if a lot of low-coherence pixels are found in the floodplain. If the flood event is exceptional, such as the one in Porto Alegre, it might miss the dark water flagging. The *a priori* approach of the SWOT algorithm was reused to extract and identify areas of low coherence.

A rasterization of the PIXC product was necessary to facilitate spatial and temporal comparisons, including pixel-to-pixel means, differences, and other metrics. This rasterization introduces bias into our data, particularly when PIXC points are poorly geolocalized, as it may introduce erroneous information into the raster. Moreover, the output raster corresponds to a geographic mean of a multi-point cloud, making it less precise than the PIXC. It is a compromise between easing the comparison between other rasters and maintaining the original precision of the data.

We compared different SWOT passes to gain a holistic understanding of the flood events from remote sensing, and also to select the proper dates that comprised the dry average for each event. The direct comparison, date to date, is simple and good for a first approach. However, this can be challenging as SWOT data may contain much noise, which is more pronounced in floodplains, where our analysis requires precision. Moreover, dry dates are scarce outside the riverbed, resulting in large, uncovered areas. This is why a dry mean raster was computed, as it reduces noise in the dry mean raster and enables the creation of a complete dry floodplain by combining multiple dates. Biases can occur around cropland and other vegetated areas, where the signal response evolves with crop growth and varying moisture states. Similarly, if the AOI is composed of a large snow cover, a dry mean with snow cover is more suitable than a dry mean computed only with dates selected during summertime. The more SWOT passes we receive, the more precise the dry mean rasters will be.

γ_{SNR} computed and used in our approach provides some missing information to the built-in classification mask. This variable adds uncertainty information to the masks computed with our methodology. The threshold of low coherence SNR permits us to discard data with low confidence in our mask within the floodplain. γ_{SNR} needs to be computed, but it provides valuable information on the entire dataset. It is noted that the higher the incidence angle, the lower the SNR coherence is. This was observed in both the Porto Alegre and Owensboro flood cases.

The three variables used in our approach, *i.e.* γ_{total}, σ_0, and $P_{coherent}$, have similar trends for the detection of flooded areas. This is observed

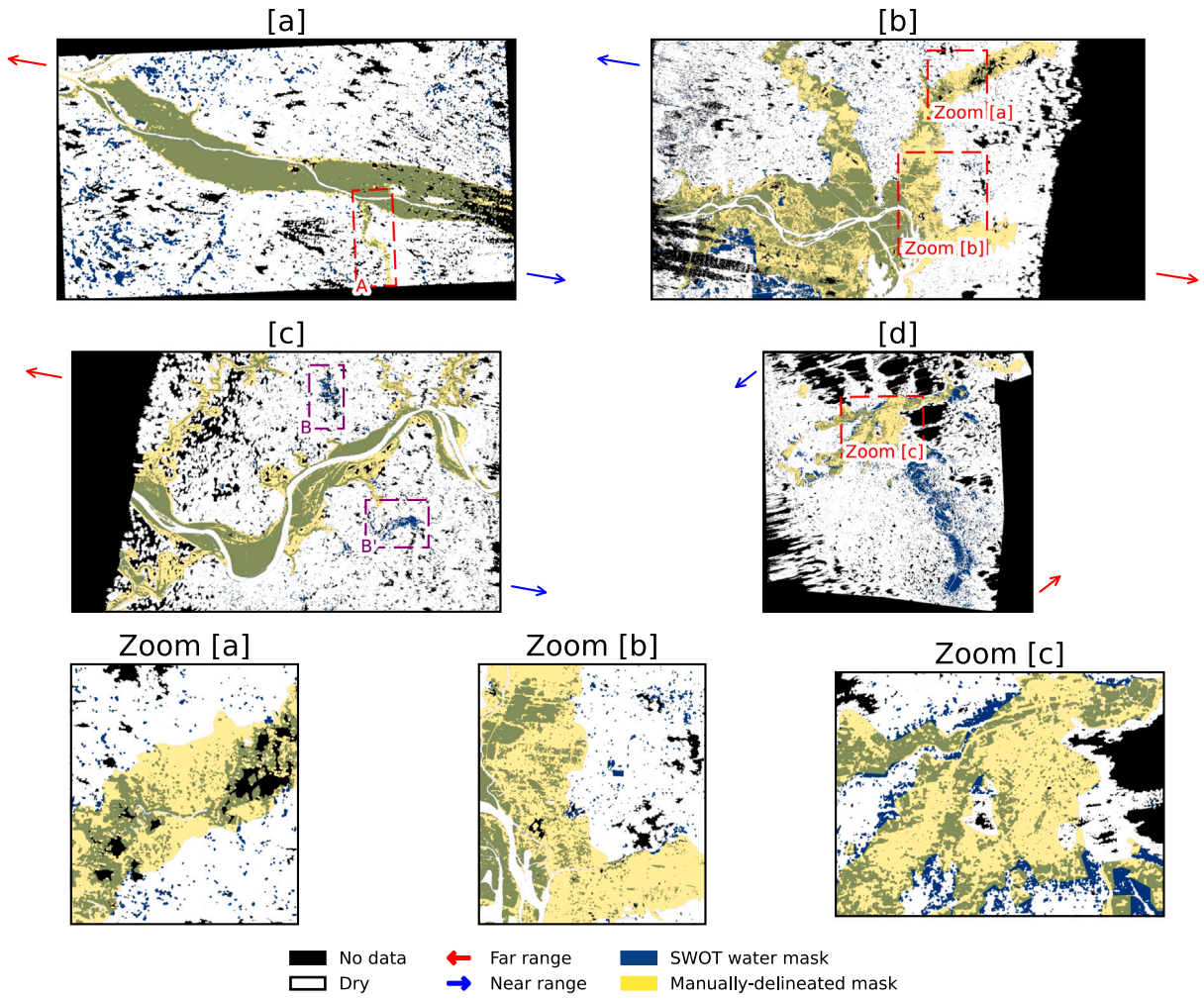

Fig. 13. Visual comparison of γ_{total} and manually-delineated water mask. Black pixels represent the "no data" value and white pixels the non-flooded pixels. (a) Chinon, France, (b) Porto Alegre, Brazil, (c) Owensboro, USA, (d) Farkadona, Greece. (Zoom [a]) Porto Alegre, Brazil: Zoom in the north urban area; (Zoom [b]) Porto Alegre, Brazil: Zoom in the south urban area; (Zoom [c]) Farkadona, Greece: Zoomed-in view of Metamórfosi city and its neighborhood. Highlighted rectangles A, B and B' mark zones of interest for further exploration and analysis.

in the four flood events, which differ in terms of season, type of flood, and type of land cover. The shape of the histograms within floodplains reveals similarities between the flood events and the land cover classes. There is a clear difference between flooded and dry histograms, which leads to an easy determination of the threshold for computing flood masks. However, when a flood occurs in an area with high soil moisture or when the flood is receding, it can be challenging to utilize SWOT data. This was the case in the Farkadona flood case. σ_0 seems to be less sensitive to soil moisture than the other variables studied for this event. In the case of high snow cover (Owensboro), a distinction between snow and the flooded areas was made again with σ_0. The snow can be viewed as bright land; therefore, some areas remain with strong uncertainty. It is challenging to classify those areas as wet snow, water under snow, or actual floodwater when the optical data indicate that they are likely wet snow or water under snow.

For flooded urban areas, the analysis is more complex but promising. The study shows that SWOT is capable of observing floods in urban areas. This analysis is specific to the Porto Alegre event. A more thorough investigation of additional flood cases would be required to better assess the behavior of SWOT data in urban areas. The land cover analysis based on interferometric coherence showed that the estimated flooded urban areas are consistent with those identified using optical data. This was not detected in the built-in classification, and only a dry mean raster was needed to extract this information. Moreover, γ_{total} is less sensitive to the incidence angle and therefore easier to use for a simple thresholding method. Some noise in the water masks is detected near cities outside the flood extent. Those areas could be discarded by using the bright land flag found in the PIXC file. However, this needs to be done after a preliminary analysis of optical or SAR data to identify urban areas that are potentially flooded.

As for σ_0 or $P_{coherent}$, flooded urban areas were not distinguishable with the histogram analysis performed. Both variables are highly intricate as $P_{coherent}$ is used to compute σ_0. Those two variables are less noisy than γ_{total} computed in our study; in some areas, they improve the detection of small bodies. Both variables are more impacted by the incidence angle than the interferometric coherence. This leads to some difficulty in thresholding homogeneously across the AOI. Some commissions and omissions were detected when the incidence angle effect was too high. A solution for improved thresholding with these variables is to perform local thresholding across the image, depending on the incidence angle. Another approach could be to normalize σ_0 and $P_{coherent}$ concerning the incidence angle to mitigate its effect.

The combined use of these three variables could lead to improved noise reduction outside the floodplain, as the divergence outside the floodplain can be directly detected. It reduces some doubt that can arise when examining only one variable, such as the wet snow phenomenon observed only on the γ_{total} mask. This hybridization may also remove details, sometimes important ones, that the three masks provide.

Those observations offer new opportunities for flood observations. While flood mapping using C-band SAR instruments is highly effective in open areas, it is known to be significantly less reliable in vegetated and urban regions. Specifically, flooded forests typically cannot be directly observed using these sensors, despite the multi-bounce effect potentially increasing SAR backscatter signals in flooded forested areas (Tsyganskaya et al., 2018). Flooded urban areas can hardly be directly detected with SAR data, but can be linked to interferometric coherence changes (Chini et al., 2019). Here, it is shown that SWOT is capable of detecting water under vegetation areas and, in some cases, urban areas using interferometric coherence.

Our approach represents the first step in flood extent extraction using the SWOT KaRIn variables. It is a method that can be made operational, although it currently needs human expertise to supervise the analysis and select floodplain areas of interest. It is an easy-to-use method once a thorough histogram analysis has been performed. The results enhance the classification already provided within the PIXC. Our approach identifies areas of uncertainty that the automatic SWOT algorithm may overlook. This is accomplished by using a specific *a priori* mask for the flood event. It provides a better understanding of the signal provided by the new KaRIn sensor.

6. Conclusion and perspectives

This study was performed to get a better understanding of the SWOT Pixel Cloud data product for flood monitoring. It shows that SWOT KaRIn instrument is capable of detecting water under vegetation and within urban areas. It also shows some weaknesses of the sensor, with sensitivity on incidence angle, soil moisture, or wind effect. To the best of our knowledge, this is the first study to integrate the SWOT PIXC data with other observations from other satellites for flood detection. The results highlight the promising potential of the SWOT mission for flood monitoring across various environments. SWOT PIXC provides high-precision flood extents, which are useful for flood monitoring and analysis.

The current built-in classification method (on SWOT-HR version C) performs well under favorable conditions—such as low dark water presence, minimal specular ringing, low wind speeds, and low soil moisture. However, it exhibits significant limitations under more complex scenarios, and careful monitoring of the mask computation is required when higher precision in flood extent mapping is needed.

Our main analysis focused on three key variables: the interferometric coherence, computed in this study, the backscattering coefficient, and coherent power, derived from single-look complex KaRIn images. These variables not only enhanced our understanding of each analyzed flood event but also contributed to a deeper insight into the capabilities of the SWOT PIXC product. Across the four studied flood events, they have been shown to effectively detect water presence in various vegetated environments as well as urban areas, such as in the Porto Alegre case study. Notably, the analysis revealed that the backscattering coefficient is less sensitive to high soil moisture conditions – such as during flood recession or in snow-covered areas – compared to the KaRIn sensor.

The final water masks obtained from SWOT variables are visually close to FloodML masks and can be very close to the manually-delineated masks. The three SWOT-derived variables provide complementary information, often offering greater precision than other sensors. This enhances and complements the global revisit capability of the multi-sensor open-data satellite fleet.

This study aimed to establish a foundation for flood monitoring using SWOT KaRIn radar variables. The proposed streamlined method shows strong potential for future advancements. A more detailed approach using the level-1 geolocalized SLC product could address the limitations of the PIXC product in dry areas, enabling more complete flood extent analysis. Implementing an automatic thresholding method using statistics from SWOT signals (e.g., σ_0 and $P_{coherent}$) could enhance detection, especially when adapted to local incidence angles. Incorporating uncertainty estimates would also support integration into data assimilation algorithms and 2D-hydraulic modeling. Furthermore, integrating SWOT data into flood monitoring systems introduces a novel perspective for hydrological analysis and emergency response, helping to identify inundated areas that may have gone undetected. Once the SWOT KaRIn instrument is better characterized, its integration into machine learning or deep learning algorithms for flood extent extraction could further accelerate analysis by combining SWOT with other Earth observation data.

CRediT authorship contribution statement

Quentin Bonassies: Writing – original draft, Visualization, Validation, Software, Resources, Methodology, Investigation, Formal analysis, Data curation, Conceptualization. **Christophe Fatras:** Writing – review & editing, Validation, Supervision, Resources, Methodology, Investigation, Funding acquisition, Formal analysis, Conceptualization. **Santiago Peña-Luque:** Writing – review & editing, Validation, Supervision, Methodology, Investigation, Funding acquisition. **Pierre Dubois:** Writing – review & editing, Validation, Supervision, Methodology. **Andrea Piacentini:** Writing – review & editing, Validation, Supervision. **Ludovic Cassan:** Writing – review & editing, Validation, Supervision. **Sophie Ricci:** Writing – review & editing, Funding acquisition. **Thanh Huy Nguyen:** Writing – review & editing.

Code availability

The algorithms used for the paper results are in the swot_for_flood Python library found in the following GitHub repository.[4] This library can be used to download SWOT Pixel Cloud data, analyze it, and extract flood extent with the presented method.

Declaration of Generative AI and AI-assisted technologies in the writing process

During the preparation of this work the lead author used ChatGPT 4o/4.1mini, DeepL and Grammarly to improve the readability and language of the first draft manuscript. After using those tools/services, all authors reviewed and edited the manuscript and take full responsibility for the content of the publication.

Declaration of competing interest

The authors declare the following financial interests/personal relationships which may be considered as potential competing interests: Quentin Bonassies reports financial support and article publishing charges were provided by French Space Agency, Collecte Localisation Satellites SA and CERFACS. The other authors declare that they have no known competing financial interests or personal relationships that could have appeared to influence the work reported in this paper.

Acknowledgments

This work was supported by the Centre National d'Etudes Spatiales (CNES), Collecte Localisation Satellites (CLS) and Centre Européen de Recherche et de Formation Avancée en Calcul Scientifique (CERFACS) [grant Number CNES 5100020268].

Appendix A. Supplementary data

Supplementary material related to this article can be found online at https://doi.org/10.1016/j.rse.2025.115101.

[4] https://github.com/quentinbns/swot_for_flood

Data availability

The raw data used within the algorithms are available on a Zenodo repository (doi: https://doi.org/10.5281/zenodo.15848842).

References

Altenau, E.H., Pavelsky, T.M., Durand, M.T., Yang, X., Frasson, R.P.d., Bendezu, L., 2021. The Surface Water and Ocean Topography (SWOT) Mission River Database (SWORD): A Global River Network for Satellite Data Products. Water Resour. Res. 57 (7), http://dx.doi.org/10.1029/2021WR030054, e2021WR030054 e2021WR030054 2021WR030054.

Andreadis, K., Coss, S., Durand, M., Gleason, C., Simmons, T., Tebaldi, N., Bjerklie, D., Brinkerhoff, C., Dudley, R., Gejadze, I., Larnier, K., Malaterre, P.o., Oubanas, H., Allen, G., Bates, P., David, C., Domeneghetti, A., Elmi, O., Marc, L.F., Prata de Moraes Frasson, R., Friedmann, E., Garambois, P.a., Gehring, J., Getirana, A., Hughes, M., Lee, J., Matte, P., Minear, J.T., Monnier, J., Muhebwa, A., Tourian, M., Pavelsky, T., Riggs, R., Rodríguez, E., Sikder, M.S., Smith, L., Stuurman, C., Taneja, J., Tarpanelli, A., Wang, J., Williams, B., Yadav, B., 2025. A First Look at River Discharge Estimation From SWOT Satellite Observations. Geophys. Res. Lett. 52 (9), http://dx.doi.org/10.1029/2024GL114185, e2024GL114185.

Bates, P.D., 2022. Flood inundation prediction. Annu. Rev. Fluid Mech. 54 (Volume 54, 2022), 287–315. http://dx.doi.org/10.1146/annurev-fluid-030121-113138.

Bates, P., De Roo, A., 2000. A simple raster-based model for flood inundation simulation. J. Hydrol. 236 (1), 54–77. http://dx.doi.org/10.1016/S0022-1694(00)00278-X.

Bertels, L., Smets, B., Wolfs, D., 2016. Dynamic Water Surface Detection Algorithm Applied on PROBA-V Multispectral Data. Remote. Sens. 8 (12), http://dx.doi.org/10.3390/rs8121010.

Biancamaria, S., Lettenmaier, D.P., Pavelsky, T.M., 2016. The SWOT Mission and Its Capabilities for Land Hydrology. Surv. Geophys. 37 (2), 307–337. http://dx.doi.org/10.1007/s10712-015-9346-y.

Bohé, A., 2023. A complete theoretical derivation of the level of random height noise in interferometric unfocused SAR swath altimetry. IEEE Trans. Geosci. Remote Sens. 61, 1–29. http://dx.doi.org/10.1109/TGRS.2023.3290850.

Bohé, A., Chen, A., Chen, C., Dubois, P., Fore, A., Molero, B., Peral, E., Raynal, M., Stiles, B., Ardhuin, F., Hay, A., Legresy, B., Lenain, L., Villas Bôas, A.B., 2025. Measuring Significant Wave Height Fields in Two Dimensions at Kilometric Scales With SWOT. IEEE Trans. Geosci. Remote Sens. 63, 1–19. http://dx.doi.org/10.1109/TGRS.2025.3551605.

Boisot, O., Pioch, S., Fatras, C., Caulliez, G., Bringer, A., Borderies, P., Lalaurie, J.C., Guérin, C.A., 2015. Ka-band backscattering from water surface at small incidence: A wind-wave tank study. J. Geophys. Res.: Ocean. 120 (5), 3261–3285. http://dx.doi.org/10.1002/2014JC010338.

Bonassies, Q., Nguyen, T.H., Cassan, L., Piacentini, A., Ricci, S., Emery, C., Fatras, C., Peña Luque, S., Rodriguez Suquet, R., 2025. Assimilation of SWOT Altimetry Data for Riverine Flood Reanalysis: From Synthetic to Real Data. URL https://arxiv.org/abs/2504.21670 arXiv:2504.21670.

Chen, C.W., 2023. A spectral model for multilook InSAR phase noise due to geometric decorrelation. IEEE Trans. Geosci. Remote Sens. 61, 1–11. http://dx.doi.org/10.1109/TGRS.2023.3272296.

Chini, M., Hostache, R., Pelich, R., Matgen, P., Pulvirenti, L., Pierdicca, N., 2019. Probabilistic Urban Flood Mapping Using SAR Data. In: IGARSS 2019 - 2019 IEEE International Geoscience and Remote Sensing Symposium. pp. 4643–4645. http://dx.doi.org/10.1109/IGARSS.2019.8898523.

Dasgupta, A., Hostache, R., Ramsankaran, R., Grimaldi, S., Matgen, P., Chini, M., Pauwels, V.R., Walker, J.P., 2021a. Chapter 12 - earth observation and hydraulic data assimilation for improved flood inundation forecasting. In: Schumann, G.J.-P. (Ed.), Earth Observation for Flood Applications. In: Earth Observation, Elsevier, pp. 255–294. http://dx.doi.org/10.1016/B978-0-12-819412-6.00012-2.

Dasgupta, A., Hostache, R., Ramsankaran, R., Schumann, G.J.-P., Grimaldi, S., Pauwels, V.R.N., Walker, J.P., 2021b. A Mutual Information-Based Likelihood Function for Particle Filter Flood Extent Assimilation. Water Resour. Res. 57 (2), e2020WR027859.

de Moraes Frasson, R.P., 2021. Using the Surface Water and Ocean Topography mission data to estimate river bathymetry and channel roughness. In: Earth Observation for Flood Applications. Elsevier, pp. 105–128.

Di Mauro, C., Hostache, R., Matgen, P., Pelich, R., Chini, M., Jan van Leeuwen, P., Nichols, N., Bloschl, G., 2021. Assimilation of probabilistic flood maps from SAR data into a coupled hydrologic-hydraulic forecasting model: A proof of concept. Hydrol. Earth Syst. Sci. 25, 4081–4097.

Durand, M., Gleason, C.J., Pavelsky, T.M., Prata de Moraes Frasson, R., Turmon, M., David, C.H., Altenau, E.H., Tebaldi, N., Larnier, K., Monnier, J., et al., 2023. A framework for estimating global river discharge from the Surface Water and Ocean Topography satellite mission. Water Resour. Res. 59 (4), e2021WR031614.

Emery, C.M., Biancamaria, S., Boone, A., Ricci, S., Rochoux, M.C., Pedinotti, V., David, C.H., 2020. Assimilation of wide-swath altimetry water elevation anomalies to correct large-scale river routing model parameters. Hydrol. Earth Syst. Sci. 24 (5), 2207–2233. http://dx.doi.org/10.5194/hess-24-2207-2020.

Fatras, C., Borderies, P., Baghdadi, N., Zribi, M., El Hajj, M., Frappart, F., Mougin, E., 2016. Radar Backscattering Coefficient Over Bare Soils at Ka-Band Close to Nadir Angle. IEEE Geosci. Remote. Sens. Lett. 13 (9), 1290–1294. http://dx.doi.org/10.1109/LGRS.2016.2582382.

Fayne, J.V., Smith, L.C., 2023. How Does Wind Influence Near-Nadir and Low-Incidence Ka-Band Radar Backscatter and Coherence from Small Inland Water Bodies? Remote. Sens. 15 (13), http://dx.doi.org/10.3390/rs15133361.

Fayne, J.V., Smith, L.C., Liao, T.-H., Pitcher, L.H., Denbina, M., Chen, A.C., Simard, M., Chen, C.W., Williams, B.A., 2024. Characterizing Near-Nadir and Low Incidence Ka-Band SAR Backscatter From Wet Surfaces and Diverse Land Covers. IEEE J. Sel. Top. Appl. Earth Obs. Remote. Sens. 17, 985–1006. http://dx.doi.org/10.1109/JSTARS.2023.3317502.

Fu, L.-L., Pavelsky, T., Cretaux, J.-F., Morrow, R., Farrar, J.T., Vaze, P., Sengenes, P., Vinogradova-Shiffer, N., Sylvestre-Baron, A., Picot, N., Dibarboure, G., 2024. The Surface Water and Ocean Topography Mission: A Breakthrough in Radar Remote Sensing of the Ocean and Land Surface Water. Geophys. Res. Lett. 51 (4), http://dx.doi.org/10.1029/2023GL107652, e2023GL107652 e2023GL107652 2023GL107652.

García-Pintado, J., Mason, D.C., Dance, S.L., Cloke, H.L., Neal, J.C., Freer, J., Bates, P.D., 2015. Satellite-supported flood forecasting in river networks: A real case study. J. Hydrol. 523, 706–724. http://dx.doi.org/10.1016/j.jhydrol.2015.01.084.

Getirana, A., Kumar, S., Bates, P., Boone, A., Lettenmaier, D., Munier, S., 2024. The SWOT Mission Will Reshape Our Understanding of the Global Terrestrial Water Cycle. Nat. Water 2 (12), 1139–1142. http://dx.doi.org/10.1038/s44221-024-00352-0.

Grimaldi, S., Li, Y., Pauwels, V.R., Walker, J.P., 2016. Remote sensing-derived water extent and level to constrain hydraulic flood forecasting models: Opportunities and challenges. Surv. Geophys. 37 (5), 977–1034.

Hamoudzadeh, A., Ravanelli, R., Crespi, M., 2024. SWOT Level 2 Lake Single-Pass Product: The L2_HR_LakeSP Data Preliminary Analysis for Water Level Monitoring. Remote. Sens. 16 (7), http://dx.doi.org/10.3390/rs16071244.

Harrigan, S., Zoster, E., Cloke, H., Salamon, P., Prudhomme, C., 2020. Daily ensemble river discharge reforecasts and real-time forecasts from the operational global flood awareness system. Hydrol. Earth Syst. Sci. Discuss. 2020, 1–22.

Hawker, L., Uhe, P., Paulo, L., Sosa, J., Savage, J., Sampson, C., Neal, J., 2022. A 30 m global map of elevation with forests and buildings removed. Environ. Res. Lett. 17 (2), 024016. http://dx.doi.org/10.1088/1748-9326/ac4d4f.

He, Z., Cai, Y., Wu, S., Xiao, Y., Li, H., and, C.-Q.K., 2025. Evaluation of swot's performance for river water level retrieval in the yangtze river basin. Int. J. Remote Sens. 1–28. http://dx.doi.org/10.1080/01431161.2025.2512162.

Hostache, R., Chini, M., Giustarini, L., Neal, J., Kavetski, D., Wood, M., Corato, G., Pelich, R.-M., Matgen, P., 2018. Near-real-time assimilation of SAR-derived flood maps for improving flood forecasts. Water Resour. Res. 54 (8), 5516–5535. http://dx.doi.org/10.1029/2017WR022205.

Jafarzadegan, K., Moradkhani, H., Pappenberger, F., Moftakhari, H., Bates, P., Abbaszadeh, P., Marsooli, R., Ferreira, C., Cloke, H.L., Ogden, F., Duan, Q., 2023. Recent Advances and New Frontiers in Riverine and Coastal Flood Modeling. Rev. Geophys. 61 (2), http://dx.doi.org/10.1029/2022RG000788, e2022RG000788 e2022RG000788 2022RG000788.

(J.P.L. D-105504), 2023. "SWOT Algorithm Theoretical Basis Document: Level 2 KaRIn High Rate Pixel Cloud (L2_HR_PIXC) Science Algorithm Software". URL https://archive.podaac.earthdata.nasa.gov/podaac-ops-cumulus-docs/web-misc/swot_mission_docs/atbd/D-105504_SWOT_ATBD_L2_HR_PIXC_20230713a_cite2.pdf.

(J.P.L. D-109532), 2024. SWOT science data products user handbook. URL https://archive.podaac.earthdata.nasa.gov/podaac-ops-cumulus-docs/web-misc/swot_mission_docs/D-109532_SWOT_UserHandbook_20240502.pdf.

Kettig, P., Baillarin, S., Blanchet, G., Taillan, C., Ricci, S., Nguyen, T.-H., Huang, T., Altinok, A., Chung, N.T., Valladeau, G., Goeury, R., Roumagnac, A., 2021. The SCO-FloodDAM Project: New Observing Strategies for Flood Detection, Alert and Rapid Mapping. In: 2021 IEEE International Geoscience and Remote Sensing Symposium IGARSS. pp. 1464–1467. http://dx.doi.org/10.1109/IGARSS47720.2021.9553036.

Laipelt, L., de Paiva, R.C., Fan, F.M., Collischonn, W., Papa, F., Ruhoff, A., 2025. SWOT reveals how the 2024 disastrous flood in South Brazil was intensified by increased water slope and wind forcing. Geophys. Res. Lett. 52 (2), http://dx.doi.org/10.1029/2024GL111287, e2024GL111287.

Lobry, S., 2017. Modèles Markoviens pour les images SAR : application à la détection de l'eau dans les images satellitaires SWOT et analyse multi-temporelle de zones urbaines (Ph.D. thesis). (2017ENST0056), Télécom ParisTech.

Marsh, C.B., Harder, P., Pomeroy, J.W., 2023. Validation of FABDEM, a global bare-earth elevation model, against UAV-lidar derived elevation in a complex forested mountain catchment. Environ. Res. Commun. 5 (3), 031009. http://dx.doi.org/10.1088/2515-7620/acc56d.

Martinis, S., Plank, S., Ćwik, K., 2018. The use of Sentinel-1 time-series data to improve flood monitoring in arid areas. Remote. Sens. 10 (4), 583.

Maubant, L., Dodd, L., Tregoning, P., 2025. Assessing the accuracy of SWOT measurements of water bodies in Australia. Geophys. Res. Lett. 52 (6), http://dx.doi.org/10.1029/2024GL114084, e2024GL114084 e2024GL114084 2024GL114084.

Meadows, M., Jones, S., Reinke, K., 2024. Vertical accuracy assessment of freely available global DEMs (FABDEM, copernicus DEM, NASADEM, AW3D30 and SRTM) in flood-prone environments. Int. J. Digit. Earth 17 (1), 2308734. http://dx.doi.org/10.1080/17538947.2024.2308734.

Moradkhani, H., Hsu, K.-L., Gupta, H., Sorooshian, S., 2005. Uncertainty assessment of hydrologic model states and parameters: Sequential data assimilation using the particle filter. Water Resour. Res. 41 (5).

Nandam, V., Patel, P., 2024. A framework to assess suitability of global digital elevation models for hydrodynamic modelling in data scarce regions. J. Hydrol. 630, 130654. http://dx.doi.org/10.1016/j.jhydrol.2024.130654.

Nguyen, T.H., Ricci, S., Fatras, C., Piacentini, A., Delmotte, A., Lavergne, E., Kettig, P., 2022a. Improvement of Flood Extent Representation With Remote Sensing Data and Data Assimilation. IEEE Trans. Geosci. Remote Sens. 60, 1–22. http://dx.doi.org/10.1109/TGRS.2022.3147429.

Nguyen, T.H., Ricci, S., Piacentini, A., Emery, C., Rodriguez Suquet, R., Peña Luque, S., 2024. Assimilation of SWOT Altimetry And Sentinel-1 Flood Extent Observations for Flood Reanalysis - A Proof-Of-Concept. In: IGARSS 2024 - 2024 IEEE International Geoscience and Remote Sensing Symposium. pp. 3163–3167. http://dx.doi.org/10.1109/IGARSS53475.2024.10641805.

Nguyen, T.H., Ricci, S., Piacentini, A., Fatras, C., Kettig, P., Blanchet, G., Peña Luque, S., Baillarin, S., 2022b. Dual State-Parameter Assimilation of SAR-Derived Wet Surface Ratio for Improving Fluvial Flood Reanalysis. Water Resour. Res. 58 (11), http://dx.doi.org/10.1029/2022WR033155, e2022WR033155 e2022WR033155 2022WR033155.

Nguyen, T.H., Ricci, S., Piacentini, A., Simon, E., Rodriguez Suquet, R., Peña Luque, S., 2023. Gaussian Anamorphosis for Ensemble Kalman Filter Analysis of SAR-Derived Wet Surface Ratio Observations. IEEE Trans. Geosci. Remote Sens. 62, http://dx.doi.org/10.1109/TGRS.2023.3338296, 1–21.

Nobre, A.D., Cuartas, L.A., Hodnett, M., Rennó, C.D., Rodrigues, G., Silveira, A., Saleska, S., 2011. Height Above the Nearest Drainage–a hydrologically relevant new terrain model. J. Hydrol. 404 (1–2), 13–29.

Oubanas, H., Gejadze, I., Malaterre, P.O., Mercier, F., 2018. River discharge estimation from synthetic SWOT-type observations using variational data assimilation and the full Saint-Venant hydraulic model. J. Hydrol. 559, 638–647. http://dx.doi.org/10.1016/j.jhydrol.2018.02.004.

Oubanas, H., Ricci, S., Malaterre, P.O., Gejadze, I., Quittard, D., Emery, C., Nguyen, T.H., Piacentini, A., Cassan, L., Bonassies, Q., 2024. Hydraulic retrievals from Data assimilation: River Observation with SWOT. In: SWOT Science Team Meeting.

Pekel, J.-F., Cottam, A., Gorelick, N., Belward, A.S., 2016. High-resolution mapping of global surface water and its long-term changes. Nature 540 (7633), 418–422. http://dx.doi.org/10.1038/nature20584.

Peral, E., Esteban-Fernandez, D., 2018. Swot mission performance and error budget. In: IGARSS 2018 - 2018 IEEE International Geoscience and Remote Sensing Symposium. pp. 8625–8628. http://dx.doi.org/10.1109/IGARSS.2018.8517385.

Peral, E., Esteban-Fernández, D., Rodríguez, E., McWatters, D., De Bleser, J.-W., Ahmed, R., Chen, A.C., Slimko, E., Somawardhana, R., Knarr, K., Johnson, M., Jaruwatanadilok, S., Chan, S., Wu, X., Clark, D., Peters, K., Chen, C.W., Mao, P., Khayatian, B., Chen, J., Hodges, R.E., Boussalis, D., Stiles, B., Srinivasan, K., 2024. Karin, the ka-band radar interferometer of the SWOT mission: Design and in-flight performance. IEEE Trans. Geosci. Remote Sens. 62, 1–27. http://dx.doi.org/10.1109/TGRS.2024.3405343.

Prudhomme, C., Zsótér, E., Matthews, G., Melet, A., Grimaldi, S., Zuo, H., Hansford, E., Harrigan, S., Mazzetti, C., de Boisseson, E., et al., 2024. Global hydrological reanalyses: The value of river discharge information for world-wide downstream applications–the example of the global flood awareness system glofas. Meteorol. Appl. 31 (2), e2192.

Rezende, I., Fatras, C., Oubanas, H., Gejadze, I., Malaterre, P.-O., Peña-Luque, S., Domeneghetti, A., 2025. Reconstruction of effective cross-sections from DEMs and water surface elevation. Remote. Sens. 17, 1020. http://dx.doi.org/10.3390/rs17061020.

Rodriguez, E., Martin, J., 1992. Theory and design of interferometric synthetic aperture radars. In: IEE Proceedings F (Radar and Signal Processing), vol. 139, (2), IET, pp. 147–159.

Rosen, P.A., Hensley, S., Joughin, I.R., Li, F.K., Madsen, S.N., Rodriguez, E., Goldstein, R.M., 2000. Synthetic aperture radar interferometry. Proc. IEEE 88 (3), 333–382.

Salameh, E., Desroches, D., Deloffre, J., Fjørtoft, R., Mendoza, E.T., Turki, I., Froideval, L., Levaillant, R., Déchamps, S., Picot, N., Laignel, B., Frappart, F., 2024. Evaluating swot's interferometric capabilities for mapping intertidal topography. Remote Sens. Environ. 314, 114401. http://dx.doi.org/10.1016/j.rse.2024.114401.

Schumann, G., Matgen, P., Cutler, M., Black, A., Hoffmann, L., Pfister, L., 2008. Comparison of remotely sensed water stages from LiDAR, topographic contours and SRTM. ISPRS J. Photogramm. Remote Sens. 63 (3), 283–296.

Simoes-Sousa, I.T., Camargo, C.M., Tavora, J., Piffer-Braga, A., Farrar, J.T., Pavelsky, T.M., 2025. The may 2024 flood disaster in southern Brazil: Causes, impacts, and SWOT-based volume estimation. Geophys. Res. Lett. 52 (4), http://dx.doi.org/10.1029/2024GL112442, e2024GL112442.

Small, D., 2011. Flattening Gamma: Radiometric terrain correction for SAR imagery. IEEE Trans. Geosci. Remote Sens. 49 (8), 3081–3093. http://dx.doi.org/10.1109/TGRS.2011.2120616.

SWOT, 2023. SWOT level 2 water mask pixel cloud data product, version 1.1. http://dx.doi.org/10.5067/SWOT-PIXC-1.1, URL https://podaac.jpl.nasa.gov/dataset/SWOT_L2_HR_PIXC_1.1.

SWOT, 2025. Surface water and ocean topography (SWOT) project - release note - version d KaRIn science data products. URL https://archive.podaac.earthdata.nasa.gov/podaac-ops-cumulus-docs/web-misc/swot_mission_docs/SWOT_VersionD_KaRIn_Products_Release_Note_20250423b.pdf.

Tsyganskaya, V., Martinis, S., Marzahn, P., Ludwig, R., 2018. SAR-based detection of flooded vegetation–a review of characteristics and approaches. Int. J. Remote Sens. 39 (8), 2255–2293. http://dx.doi.org/10.1080/01431161.2017.1420938.

Twele, A., Cao, W., Plank, S., Martinis, S., 2016. Sentinel-1-based flood mapping: a fully automated processing chain. Int. J. Remote Sens. 37 (13), 2990–3004.

UNDRR, 2021. The human cost of disasters: an overview of the last 20 years (2000–2019). URL https://www.preventionweb.net/files/74124_humancostofdisasters20002019reportu.pdf.

Wongchuig-Correa, S., de Paiva, R.C.D., Biancamaria, S., Collischonn, W., 2020. Assimilation of future SWOT-based river elevations, surface extent observations and discharge estimations into uncertain global hydrological models. J. Hydrol. 590, 125473.

Yu, L., Zhang, H., Gong, W., Ma, X., 2024. Validation of Mainland Water Level Elevation Products From SWOT Satellite. IEEE J. Sel. Top. Appl. Earth Obs. Remote. Sens. 17, 13494–13505. http://dx.doi.org/10.1109/JSTARS.2024.3435363.

Zanaga, D., Van De Kerchove, R., Daems, D., De Keersmaecker, W., Brockmann, C., Kirches, G., Wevers, J., Cartus, O., Santoro, M., Fritz, S., Lesiv, M., Herold, M., Tsendbazar, N.-E., Xu, P., Ramoino, F., Arino, O., 2022. ESA WorldCover 10 m 2021 v200. http://dx.doi.org/10.5281/zenodo.7254221.